AFOSR FINAL REPORT

F49620-96-1-0408

Electrohydrodynamic Control of Thin Film Evaporative Heat Transfer in Micro Groove Arrays

Kevin P. Hallinan and A. Reza Kashani
University of Dayton
Department of Mechanical Engineering
Dayton, Ohio 45469-0210

April 06, 2000

REPORT DOCUMENTATION PAGE

AFRL-SR-BL-TR-00-

0316

1. AGENCY USE ONLY *(Leave blank)*	2. REPORT DATE	3. REPORT TYPE AND DATES COVERED
	April 6, 2000	FINAL TECHNICAL REPORT 1 Aug 96 - 31 Jul 99

4. TITLE AND SUBTITLE
ELECTROHYDRODYNAMIC CONTROL OF THIN FILM EVAPORATIVE HEAT TRANSFER IN MICRO HEAT PIPE ARRAYS

5. FUNDING NUMBERS
F49620-96-1-0408

63739E
A564/38

6. AUTHOR(S)
KEVIN P. HALLINAN, AND A. REZA KASHANI

7. PERFORMING ORGANIZATION NAME(S) AND ADDRESS(ES)
UNIVERSITY OF DAYTON
DEPARTMENT OF MECHANICAL ENGINEERING
DAYTON, OH 45469-0210

8. PERFORMING ORGANIZATION REPORT NUMBER

9. SPONSORING/MONITORING AGENCY NAME(S) AND ADDRESS(ES)
AIR FORCE OFFICE OF SCIENTIFIC RESEARCH
801 N. RANDOLPH STREET, ROOM 732
ARLINGTON, VA 22203-1977

10. SPONSORING/MONITORING AGENCY REPORT NUMBER

11. SUPPLEMENTARY NOTES

12a. DISTRIBUTION AVAILABILITY STATEMENT
APPROVED FOR PUBLIC RELEASE, DISTRIBUTION IS UNLIMITED

12b. DISTRIBUTION CODE

13. ABSTRACT *(Maximum 200 words)*

Research has been conducted toward the development of electro-hydrodynamically (EHD) driven micro heat pipe arrays. This research has focused on the following:

· Completion of the experimentation and analysis of EHD augmented micro heat pipe arrays using dielectrophoretic forces.
· Development and analysis of ion-drag pumped micro heat pipe arrays.
· Demonstrated active thermal control with ion-drag pumped micro heat pipe arrays for cyclic heat loadings in excess of 100 W/cm2.

The research has demonstrated that the forces induced via the ion-drag mechanism can be appreciably greater than by the dielectrophoretic effect, i.e., force induced as a result of an electric field present at a liquid-vapor interface. Moreover, because the ion-drag force can be generated within the heat pipe fluid at any location, the localized electric field can be better isolated from the heat source. In the case of electronics cooling, this is particularly critical.

14. SUBJECT TERMS	15. NUMBER OF PAGES
	47
	16. PRICE CODE

17. SECURITY CLASSIFICATION OF REPORT	18. SECURITY CLASSIFICATION OF THIS PAGE	19. SECURITY CLASSIFICATION OF ABSTRACT	20. LIMITATION OF ABSTRACT
U	U	U	

Table of Contents

I. Synopsis

Research has ~~continued~~ been conducted toward the development of electro-hydrodynamically (EHD) driven micro heat pipe arrays. This research has focused on the following:

- Completion of the experimentation and analysis of EHD augmented micro heat pipe arrays using dielectrophoretic forces.
- Development and analysis of ion-drag pumped micro heat pipe arrays.
- Demonstrated active thermal control with ion-drag pumped micro heat pipe arrays for cyclic heat loadings in excess of 100 W/cm^2.

The research has demonstrated that the forces induced via the ion-drag mechanism can be appreciably greater than by the dielectrophoretic effect, i.e., force induced as a result of an electric field present at a liquid-vapor interface. Moreover, because the ion-drag force can be generated within the heat pipe fluid at any location, the localized electric field can be better isolated from the heat source. In the case of electronics cooling, this is particularly critical.

II. Primary Goal

The primary objective of the research has been to achieve active thermal control of a heated substrate for heat loadings in excess of 10 W/cm^2 using electrostatically induced forces within a micro heat pipe array.

III. Objectives

To realize this goal, our research had the following objectives:

- Investigate the possibility of using electric fields to augment the heat transport capability of a micro heat pipe device relying upon the dielectrophoretic effect --- e.g., the force induced by applying an electric field across a liquid-vapor interface. An analytical prediction of the transport capability of this type of electro-hydrodynamically (EHD) pumped micro heat pipe device was to be completed.
- Investigate the possibility of using electric fields to augment the heat transport capability of a micro heat pipe device relying upon ion-drag pumping. An analytical prediction of the transport capability of this type of EHD pumped micro heat pipe device was to be completed.
- Choose the best of these two alternative designs and determine its potential for actively controlling the temperatures of substrates subjected to cyclical heat loadings.

IV. Work Performed

The following sections describe the research that has been completed toward these objectives. The first details the accomplishments made in the development of electrohydrodynamically augmented micro heat pipe arrays. The second details the accomplishments made in the development of ion drag assisted micro heat pipes and the success achieved toward using these for active thermal control for variable heat load.

Experimental and Analytical Studies of the Maximum Heat Transport Capacity in Electrohydrodynamically Enhanced Micro Heat Pipes

Abstract

An experimental investigation was conducted to evaluate the potential benefits of electrohydrodynamic (EHD) forces on the operation of micro heat pipes. In these experiments, electric fields were used to orient and guide the flow of the dielectric liquid within the micro heat pipe from condenser to evaporator. The experiments indicate the heat transport capability of the EHD micro heat pipes is increased by up to 6 times of that of conventional ones. In parallel, an analytical model was developed to predict the maximum heat transport capability for various electric field intensities and micro heat pipe geometries. The analytical model agrees well with the experimental results for the geometry studied experimentally. The model shows that large pore sizes are optimal from a heat transport capacity perspective. Finally, a critical assessment of the experimental results suggest an alternative design capable of achieving as much as a 240 times improvement in the heat transport capacity in comparison to traditional micro heat pipes.

Introduction

Micro heat pipe devices have drawn much attention for their promise to dissipate high power densities since Cotter (1984) first proposed them. Their promise comes from the effective heat transport associated with phase change and their small geometry. In general, a micro heat pipe consists of a small noncircular channel that utilizes sharp angled corner regions as liquid arteries (wick structure) to provide liquid flow from the condenser to the evaporator region. The heat applied to the evaporator end vaporizes the working liquid in that region, forcing it to the cooler end where it condenses and gives up the latent heat of vaporization. A typical micro heat pipe has a hydraulic diameter ranging from 10 μm to several mm and a length of up to several centimeters. By definition, a micro heat pipe requires the Bond number ($Bo = \rho g R_h^2/\sigma$) to be on the order 1 or less. Many studies have been conducted on different kinds of micro heat pipe (Babin and Peterson, 1990; Longtin, et al., 1994; Khrustalev and Faghri, 1995; Ma and Peterson, 1996, 1998; Peterson and Ma, 1999). To date the maximum heat flux dissipated with these devices has been 60 W/cm^2 (Cao el at., 1993).

One of the factors which limits the heat transport capacity of micro heat pipes is the large viscous losses associated with the transport of the liquid from the condenser to the evaporator (Peterson, 1994 and Faghri, 1995). As the heat input is increased, these losses increase. At large heat inputs, the liquid flow rate cannot sustain the evaporation. When this occurs the evaporator region is said to 'dry out'. This limitation is called capillary limitation. Another shortcoming is that conventional micro heat pipes are passive in nature and do not allow for active control of the system temperature. Thus, as the heat input increases, so too does the temperature of the heat source.

The present research is premised on the assumption that both augmentation of the heat transport capacity and active thermal control of micro heat pipes can be achieved through the application of a static electric field. When an electric field is strategically

applied within micro heat pipes at the liquid-vapor interfaces that are internally present, dielectrophoretic electrohydrodynamic forces can be induced due to the discontinuity of the electrical permittivity of the medium. These forces can contribute to a pressure jump condition at the interface, effectively reducing the liquid pressure in the region affected by the field. This pressure reduction can be used to augment the flow of liquid from the condenser to the evaporator region.

Jones (1973) first proposed replacing the capillary wick structure in a heat pipe with electrodes. The concept was demonstrated successfully by Jones and Perry (1974a) and Jones (1974b). Their results showed that the electric field was able to communicate working fluid between the condenser and the evaporator enabling the functioning of the heat pipes, but the performance was poor in comparison to the existing capillary driven heat pipes. Loehrke and Debs (1975) improved the EHD heat pipe of Jones and Perry and were able to achieve equivalent thermal performance of conventional axial-groove heat pipes. More recently, Bryan and Seyed-Yagoobi (1997) performed an experimental study on monogroove EHD heat pipe. About 100% enhancement in the heat transport capacity was achieved in their experiments as a result of the EHD pumping.

Hallinan et al. (1998) conducted experimental studies on electrohydrodynamic micro heat pipe arrays. Their experiments were conducted on a micro heat pipe array having multiple parallel 1 mm (wide) by 0.6 mm (deep) grooves. The results of their experiments showed that for low heat input the electric field had little effect on heat transport as capillarity was sufficient to sustain liquid to the evaporator. However, at heat inputs sufficient to cause evaporator dry out, the application of an electric field had the effect of reducing the heat source temperature.

Based on the promising initial work of Hallinan et al.(1998), more detailed experiments were conducted to more completely identify the factors that influence the heat transport capacity of EHD assisted micro heat pipes. Additionally, to better generalize the results for various fluids and micro heat pipe geometry, an analytical model of an EHD assisted micro heat pipe is developed which can be used to predict the maximum heat transport capacity and the optimum geometry.

EHD Assisted Micro Heat Pipe Concept

Although the electrohydrodynamic heat pipe was introduced many years ago and various descriptions have since been studied, the application to micro heat pipe systems is new. The fundamental operating principles of electrohydrodynamic (EHD) micro heat pipes are described as follows. When an electric field is applied within the heat pipe, if the working fluid is a dielectric, the molecules in the working fluid are polarized, causing their negatively charged electron cloud to be displaced toward the high voltage electrode relative to the position of their positively charged nuclei. Since the kinetic energy of the liquid molecules is much less than that of vapor molecules at equivalent temperature, the polarizing influence of the electric field is substantially greater in the liquid phase than in the vapor phase. Because all systems tend toward minimum energy, when an electric field is applied within heat pipes, the liquid within tends to fill the regions of higher electric field intensity. If the electrodes are strategically placed in the evaporator, then liquid will be drawn there while vapor will be displaced toward the condenser.

Based on this reasoning, in the present experimental model the electrodes were located in the evaporator where the working liquid is needed. These electrodes were

located along every other groove. Fig. 1(a) shows an overview of the micro heat pipe used in the present model. As well, the liquid orientation within the micro heat pipe is shown in the absence of an electric field with a slight inclination angle. Fig. 1(b) illustrates the liquid orientation with the electric field applied, with liquid filling the grooves where the electrodes are present and receding in the grooves without electrodes. For the electrode configuration employed, the localized electric field in the evaporator draws liquid into the evaporator. A long wavelength instability (Melcher, and Smith, 1969) causes the liquid to bridge, producing a "slug" of liquid beneath the electrodes. If the vapor bubble trapped in the evaporator leg is small, liquid flow losses to the evaporator are reduced in comparison to Fig. 1(a)'s configuration. As such, the heat transport capacity of the micro heat pipe can be increased. Note that the adjacent grooves, not covered by electrodes, provide a vapor return flow path. Thus a heat transfer loop is formed within the EHD micro heat pipe, potentially offering a very efficient means for heat transport.

Modeling of EHD Heat Micro Pipes

The model developed here follows that of Ma and Peterson (1998) for a conventional micro heat pipe, differing primarily in the inclusion of dielectrophoretic EHD forces. The model is subject to the following assumptions: steady-state flow, constant fluid properties, a nearly horizontal configuration, constant meniscus radius of curvature at a given axial location, constant vapor temperature, and constant surface tension. Also, only axial variations in temperature and meniscus shape are considered.

At steady state, the operation of EHD micro heat pipes requires that the pressure potential provided by the combination of electrohydrodynamic forces and capillarity be greater than the sum of all the pressure drops occurring throughout the liquid and vapor flow paths. This requirement can be expressed as (Peterson, 1994)

$$\Delta P_{EHD} + \Delta P_c \geq \Delta P_v + \Delta P_l + \Delta P_+ + \Delta P_{slug} \qquad (1)$$

where ΔP_+ is the normal hydrostatic pressure drop which can be neglected in the present model because of the assumed horizontal operation, and ΔP_{slug} is the pressure gradient in the liquid slug located beneath the electrodes. Here, the electrohydrodynamic pumping pressure ΔP_{EHD} can be found from Maxwell stress tensor (Crowley, 1986)

$$T_{ij} = \varepsilon E_i E_j - \frac{\varepsilon}{2}(E_k E_k)\delta_{ij} \qquad (2)$$

where δ_{ij} is the Kronecker delta. In the present model, the main electric field direction is defined as y, so E_x and E_z are much less than E_y. Thus, the stress tensor is given as $T_{yy} = 1/2 \cdot \varepsilon_l E^2 = P$. At the interface in the liquid phase, $P_l = 1/2 \cdot \varepsilon_l E^2$, and in the vapor phase, $P_v = ½ \varepsilon_v E^2$. Here the electric field is assumed to be uniform. Therefore, the pressure discontinuity at the liquid-vapor interface due to the applied electric field is

$$\Delta P_{EHD} = \frac{1}{2}(\varepsilon_l - \varepsilon_v)E^2 \qquad (3)$$

Here ΔP_{EHD} acts normally from liquid to vapor.

The pressure drops in the micro heat pipe array are schematically illustrated in Fig. 2 and they are determined as follows. Based on the Laplace-Young equation, ΔP_c arises from the capillary pressure differences between the evaporator and condenser ends and can be written as:

$$\Delta P_c = \sigma\left(\frac{1}{r_{c,e}} - \frac{1}{r_{c,c}}\right) \tag{4}$$

where $r_{c,e}$ is the minimum meniscus radius of the curvature in the evaporator and $r_{c,c}$ is the average meniscus radius of curvature occurring in the condenser. For the other terms in equation (1), the expressions suggested by Ma and Peterson (1998) are used. The minimum meniscus radius in the evaporator is defined as

$$r_{c,e} = \frac{3\sigma}{4\cdot\left(\frac{\sigma}{r_{c,c}} + \Delta P_v + \rho_l g L \sin\psi\right)} \tag{5}$$

The average meniscus radius in the condenser is set equal to half of the width of channel.

The vapor pressure drop, ΔP_v, is given as below based on momentum conservation

$$\Delta P_v = \frac{f_v \cdot \mathrm{Re}_{h,v}\,\mu_v}{2(r_{h,v})^2 A_v \rho_v \lambda} L_{eff}\, q \tag{6}$$

The liquid pressure drop, ΔP_l, is given as

$$\Delta P_l = \left(\frac{f_l \cdot \mathrm{Re}_{h,l}\,\mu_l L_{eff}}{2C_1(C^* C_2 r_{c,e})^4 \rho_l \lambda}\right)\cdot q \tag{7}$$

where C_1 and C_2 are coefficients depending only on the channel angle of the groove and the contact angle of the liquid, and C^* may be determined as

$$C^* = \frac{1}{2}\left(1 + \frac{r_{c,c}}{r_{c,e}}\right) \tag{8}$$

However, the application of electric field make the wick structure of EHD micro heat pipe different from the conventional one, resulting in thicker film and slugs. Therefore the coefficient C^* is determined based on experimental data.

As seen in Fig. 1(b) the working liquid was drawn to the region of electric field forming liquid slugs beneath the electrodes. The flow losses in this slug, ΔP_{slug}, can be derived for laminar flow in a square channel filled with liquid:

$$\Delta P_{slug} = \frac{12\,\mu_l}{w a^3 \rho_l \lambda} L_{slug}\, q \tag{9}$$

where L_{slug} is the length of the slug on both side of the trapped vapor bubble.

Substituting all the above expressions into Eq. (1) and rearranging, a relationship between thermal throughput q and electric field intensity E is found as follows

$$q = \frac{1}{M}\left[\varepsilon_0(\varepsilon_l - \varepsilon_v)\frac{E^2}{2} + \sigma\left(\frac{1}{r_{c,e}} - \frac{1}{r_{c,c}}\right)\right] \tag{10}$$

In this equation, M can be considered as a parameter depending upon the geometry of the micro heat pipe and the properties of the working fluid, and it is expressed as

$$M = \frac{12\mu_l L_{slug}}{w a^3 \rho_l \lambda} + \frac{f_v \mathrm{Re}_{h,v}\,\mu_v L_{eff}}{2 r_{h,v}^2 A_v \rho_v \lambda} + \frac{f_l \mathrm{Re}_{h,l}\,\mu_l L_{eff}}{2C_1(C^* C_2 r_{e,e})^4 \rho_l \lambda} \tag{11}$$

Once the applied electric field intensity and the minimum meniscus radius of the curvature occurring in the evaporator are given, the maximum heat transport capacity can be predicted by Eq. (10).

Based upon the present EHD micro heat pipe, the coefficients C_1 and C_2 are equal to 1.195 and 0.45 respectively, which were determined according to the geometry of the grooves and the contact angle of the liquid. C^* in Eq. (7) is adjusted to be 1.68 to obtain best correspondence between the model predictions and experimental results. An value of 16 was taken for $f_v \cdot Re_{h,v}$ and 15 for $f_l \cdot Re_{h,l}$ according to the geometry of the duct (Bejan, 1995).

Experiments

The micro heat pipe array used in the present experiments was manufactured of a 1 mm thick glass slide. It was 28 mm long and composed of 7 parallel grooves that terminated in plenums on both ends. The grooves and plenum were machined via an ultrasonic milling process. The cross section of each channel was 1 mm wide by 0.6 mm deep and the spacing between the channels was 1 mm. Five such arrays were evaluated in the experiments.

Several shapes and locations of electrodes were utilized. The configuration producing the best results is as shown in Fig. 1. The electrode pair sandwiches the groove in the evaporator section as shown in Fig. 1c. From Fig. 1c, it can be seen that the high voltage electrodes were directly attached to the 1 mm thick cover slide adhered to the open side of the grooves; hence the electrode was in intimate contact with the liquid. The ground electrodes were attached to the exterior surface of the grooved slide. Therefore, the spacing between two electrodes of different levels is 1 mm.

Heat was input to the heat pipe array via an electric resistance heater element located just at the end of channels on the evaporator side as shown in Fig. 1. Heat was rejected by pumping 5 ^{0}C deionized water through a cooling jacket attached to the micro heat pipe array on the condenser side. The entire facility was insulated with 5 cm of ceramic fiber insulation to ensure that all heat was rejected through the cooling jacket. Heat losses were estimated to be less than 5% of the total heat input.

Five calibrated thermocouples were attached to the micro heat pipe array with thermally conducting epoxy. These thermocouples were distributed along the central channel with spacing of 5.5 mm. They were used to monitor micro heat pipe temperature in the tests. Every test continued until steady state was reached, usually taking 24 to 30 minutes. The uncertainty associated with the temperature measurement was less than ± 0.2 ^{0}C.

The working fluid used in the experiments was pentane, a dielectric fluid with high vapor pressure. The micro heat pipe array was posed at 9^0 tilt angle, with the evaporator elevated above the condenser. This initial bias was only necessary at start-up. The applied electric field intensities were 4, 6, 8 and 9.5 kilovolts per millimeter. Tests without electric field were also conducted to serve as a baseline for tests conducted with electric field applied. The heat inputs considered were 1 Watt, 1.5, 2, 2.5 and 3 Watts respectively for each of the five different electric field intensities. The micro heat pipes were filled with pentane with 30%, 40%, 52% and 60% liquid volume fractions at ambient conditions.

The experimental test procedure was as follows. First the deionized water was pumped through the cooling jacket. The electric field and heat input were established simultaneously. The wall temperatures were monitored until steady state was reached, at which time the heat input and electric field were discontinued. Some experiments were conducted with the micro heat pipe visible. The transparent structure permitted visualization of the internal fluid orientation. A Hi-8 camera was used to provide a video record of the operation in order to better understand its functioning.

Results and Discussion

The experiments conducted were mainly focused on investigating the influence of the applied electrostatic field on the maximum heat transport capacity. The experimental maximum heat transport capacity was determined in the following way. For an applied electric field strength and heat input, the experiment continued until the wall temperature reached a steady-state value. When the maximum heat transport capacity was reached, dry-out conditions in the evaporator caused the evaporator temperature to rise rapidly. The model permitted prediction of the maximum heat transport capacity for various electric field intensities. These predictions were determined using Eq. (10). Both the experimental results and the model predictions for the maximum heat transport capacity as a function of the electric field intensity are presented in Fig. 3. Good agreement between predicted and experimental values is achieved. In Fig. 3 both experimental data and model predictions show that increasing electric field intensity causes an increase in the maximum heat transport capacity. Most significantly the experimental results suggest about a sixfold improvement in the maximum heat transport capacity at the greatest electric field considered (9.5 kV/mm), above which corona discharge was evident.

In evaluating the heat transport capacity using Eq. (10), it is found that with an increase in the electric field intensity the proportion of the electrohydrodynamic potential to the total driving potential increases. This increase in heat transport capacity with electric field is better visualized by looking at the relative importance of the EHD driving force to capillarity as a function of the electric field, as shown in Table 1. Here ΔP_{total} represents the total driving pressure. It can be seen from Table 1 that the EHD potential becomes the dominant driving force at high electric fields, constituting 87.3 % of the driving potential at an electric field of 8 kV/mm.

Having established the accuracy of the model in predicting the performance of one EHD micro heat pipe, the developed model can also be used to analyze geometrical and parametric variations of the EHD micro heat pipes. Setting the spacing between the grooves, d, to be two times the width of a groove, i.e. $d = 2w$ and L, the length of a channel, the relationship between the maximum heat transport capacity and the groove width is revealed to be $q \propto w^4$ and is plotted in Fig. 4. In this figure the electric field is 8 kV/mm and the micro heat pipe length is 22 mm. Fig. 4 shows that the maximum heat transfer capacity of EHD micro heat pipes is achieved when the groove width is maximized. Note that this would only be true for Bond numbers less than unity. The relationship between q and w for zero electric field is approximately $q \propto w^2$. Interestingly, EHD micro heat pipes receive more benefit from larger pore sizes than conventional micro heat pipes.

The relationship between the maximum heat transfer capacity and the length L is also obtained at 8 kV/mm and is plotted in Fig. 5. This figure shows the effect of micro heat pipe length for different groove widths on maximum heat transport capacity. Combined these results suggest that a wider and shorter micro heat pipe is optimum. Similar conclusions were drawn by Longtin et al. (1994) for conventional micro heat pipes.

Closer inspection of the model predictions finds that the vapor pressure drop only accounts for 0.42 % and the losses in the liquid slug pressure drop respectively the 0.2 % of the total pressure. Nearly all of the pressure drops are confined to the liquid film surrounding the trapped vapor bubble in the liquid supply channels (see Fig 2). This result indicates that if the trapped vapor bubble can be eliminated, much greater heat transport capacity can be obtained. This ideal condition is achieved if the electrodes fully cover the liquid supply channels as shown in Fig. 6. When electric field is applied, the channel covered by electrodes is filled with liquid. In this scenario, the pressure drops are as illustrated is Fig. 6b. In this case, Eq. (1) becomes

$$\Delta P_{EHD} + \Delta P_c \geq \Delta P_v + \Delta P_{slug} \qquad (12)$$

The heat transport capacity is then expressed as

$$q = \frac{1}{M'}\left[\varepsilon_0(\varepsilon_l - \varepsilon_v)\frac{E^2}{2} + \sigma\left(\frac{1}{r_{c,e}} - \frac{1}{r_{c,c}}\right)\right] \qquad (13)$$

where M' is expressed as

$$M' = \frac{12\mu_l L_{slug}}{wa^3\rho_l\lambda} + \frac{f_v \mathrm{Re}_{h,v}\,\mu_v L_{eff}}{2r_{h,v}^2 A_v \rho_v \lambda} \qquad (14)$$

A comparison of the model predictions on heat transport capacity for a fully and partially liquid filled evaporator channel as a function of electric field is demonstrated in Fig. 7. Here, the fully liquid filled means the whole channel beneath the electrode was fully filled with liquid when electric field applied as shown in Fig. 6; and the partially liquid filled means the channel beneath the electrode was partially (40-50%) filled with liquid as shown in Fig. 1(b). Clearly, elimination of the entrapped vapor bubble can substantially increase the heat transport capacity of the micro heat pipe. In this case, up to a 240 fold increase in the heat transport capacity is predicted.

Experimentally, electrodes were fashioned to cover the whole liquid supply channels. The micro heat pipe was charged with a 50% liquid volume fraction at ambient conditions as shown in Fig.6(a). The maximum heat transport capacity measured experimentally was observed to be substantially less than the very optimistic predictions shown in Fig. 8. The reason for the poor performance was a function of the manufacture of the micro heat pipes. As shown in Fig. 1(c) only the high level electrode was in direct contact with the liquid in the micro heat pipe. A layer of glass was present between the ground level electrode and the liquid. During operation many free charges in the liquid are advected toward the evaporating interface. Those positive charges collecting on the glass surface near this interface are unable to dissipate through conduction through the glass. Therefore, an electric double layer forms to effectively reduce the electric field intensity of the evaporating interface as shown in Fig. 9, diminishing the driving force. This phenomena, however, is not indicative of the inherent failure of this concept. Rather it suggests a remedy that should be addressed in future design. The high voltage and

ground level electrodes in the evaporating channels should be in intimate contact with the liquid. As well, the vapor return line should be completely shielded from the electric field. Such a design is expected to be the optimum one.

Conclusions

A mathematical model to predict the maximum heat transport capacity of electrohydrodynamic micro heat pipes versus electric field intensity is presented. Good agreement is achieved in comparing the predicted value with the experimental data. Equation (10) indicates that increasing applied electric field can increase the maximum heat transport capacity of EHD micro heat pipes since at high level electric field, the EHD driving force became dominant. The optimum geometry of the EHD micro heat pipe can also be predicted using Eq. (10). The prediction indicates that the optimum EHD micro heat pipe is short and wide with the requirement that the Bo number be less than one. An ideal configuration of the EHD micro heat pipe is predicted by Eq. (10). The ideal EHD micro heat pipe model should have specially shielded vapor return channels for the vapor to reach condenser rapidly. Eq. (10) can be used to predict the performance of EHD micro heat pipes and aid the future design of the pipes.

Nomenclature

A = cross-sectional area, m^2
a = channel depth, m
C = coefficient
d = width of pipe + space between pipes, m
E = electric field intensity, V/m
f = friction factor
g = gravitational acceleration, m/s^2
L = length, m
L_{eff} = effective length, m
M = parameter defined in Eq. (10)
P = pressure, N/m^2
Q = total heat input into device, Watts
q = heat transport for one channel, Watts
Re = Reynolds number
T = temperature, K
w = channel width, m
ε = permittivity
ρ = density, kg/m^3
σ = surface tension, N/m
λ = latent heat of vaporization, J/kg
μ = viscosity, Ns/m^2

ψ = tilt angle

Subscripts

c = capillary

EHD = electrohydrodynamic

e = evaporator
h = hydraulic
l = liquid
max = maximum
v = vapor

Reference:

Babin, B. R., Peterson, G. P., and Wu, D., 1990, "Steady-State Modeling and Testing of a Micro Heat Pipe," ASME JOURNAL of HEAT TRANSFER, Vol. 112, pp. 595-601.

Bejan, A., 1995, *Convection Heat Transfer*, John Wiley & Sins, New York, pp.100-105.

Bryan, J. E. and Seyed-Yagoobi, J., 1997, "Heat Transport Enhancement of Monogroov Heat Pipe with Electrohydrodynamic Pumping", Journal of Thermophysics and Heat Transfer, Vol. 11, No. 3, pp. 454-460.

Cao, Y., Faghri, A., and Mahefkey, E. T., 1993, "Micro/Miniature Heat Pipes and Operating Limitations", ASME Annual Meeting, Atlanta, GA, HTD-Vol.236, pp. 55-62.

Cotter, T. P., 1984, "Principles and Prospects for Micro Heat Pipes," *Proceeding of the 5th International Heat Pipe Conference,* Tsukuba, Japan, pp. 328-335.

Crowley, J. M., Fundamentals of Applied Electrostatics, John Wiley & Sons, New York, 1986, pp. 161-167.

Dean, J. A., *Lange's Handbook of Chemistry*, 14th edition, McGraw-Hill, Inc., 1992, pp. 5.119 and 8.163.

Faghri, A., 1995, *Heat Pipe Science and Technology*, Taylor & Francis, Washington, DC, Chapter 10.

Hallinan, K. P., Bhagat, W. W., Kashaboina, B., and Kashani, R., 1998, "Electro-hydrodynamic Augmentation of Heat Transport in Micro Heat Pipe Arrays," presented at the 1998 ASME-ISE, Anaheim, California, November.

Jones, T. B., 1973, "Electrohydrodynamic heat pipes", International Journal of Heat and Mass Transfer, Vol. 16, pp. 1045-1048.

Jones, T. B., and Perry, M. P., 1974a, "Electrohydrodynamic heat pipe experiments," Journal of Applied Physics, Vol. 45, pp. 2129-2132.

Jones, T. B., 1974b, "An electrohydrodynamic heat pipe," Mechanical Engineering Vol. 96, January 1974, pp. 27-32.

Khrustalev, D. and Faghri, A., 1995, "Heat Transfer During Evaporation on Capillary-Grooved Structures of Heat Pipes," ASME JOURNAL of HEAT TRANSFER, Vol. 117, pp. 740-747.

Loehrke, R. I., and Debs, R. J., "Measurements of the Performance of an Electrohydrodynamic Heat Pipe," AIAA Paper75-659, May 1975.

Longtin, J. P., Badran, B., and Gerner, F. M., 1994, "A One-Dimensional Model of a Micro Heat Pipe During Stead-State Operation," ASME JOURNAL of HEAT TRANSFER, Vol. 116, pp. 709-715.

Ma, H. B., and Peterson, G. P., 1996, "Experimental Investigation of the Maximum Heat Transport in Triangular Grooves," ASME JOURNAL of HEAT TRANSFER, Vol. 118, pp. 740-746.

Ma, H. B., and Peterson, G. P., 1998, "The Minimum Meniscus Radius and Capillary Heat Transport Limit in Micro Heat Pipes," ASME JOURNAL of HEAT TRANSFER, Vol. 120, pp. 227-233.

Melcher, J. R., and Smith, C. V., 1969, "Electrohydrodynamic Charge Relaxation and Interfacial Perpendicular-Field Instability," The Physics of Fluids, Vol. 12, pp.778-790.

Peterson, G. P.,1994, *An Introduction to Heat Pipes*. John Wiley & Sons, Inc., New York, Chapter 6.

Peterson, G. P., and Ma, H. B., 1999, "Temperature Response of Heat Transport in a Micro Heat Pipe," ASME JOURNAL of HEAT TRANSFER, Vol. 121, pp. 438-445.

Electrodes

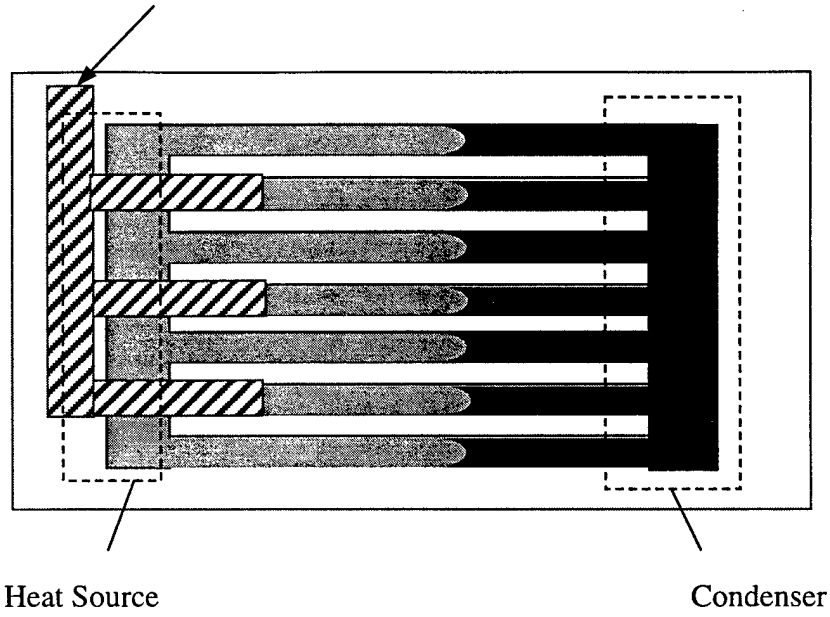
Heat Source
Condenser

(a)

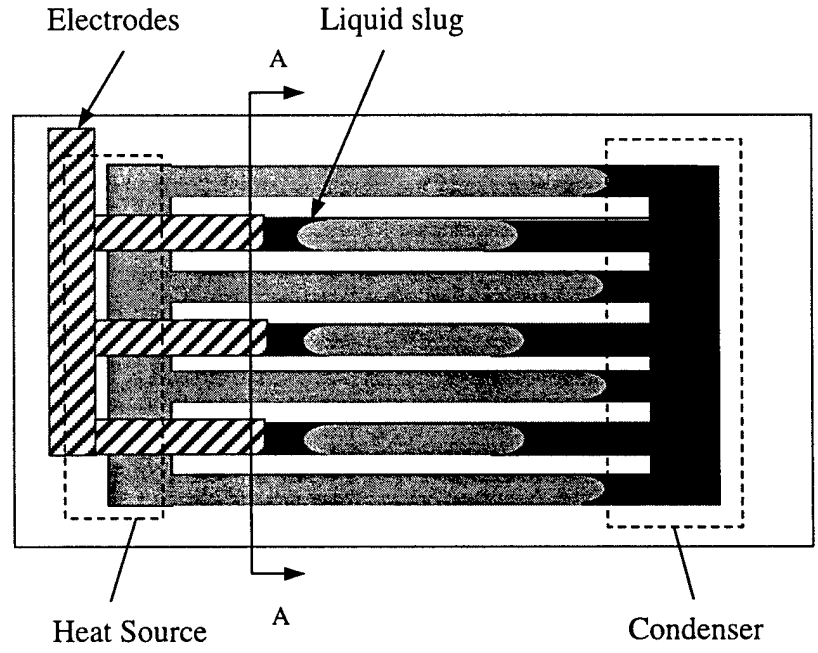
Electrodes
Liquid slug
A
A
Heat Source
Condenser

(b)

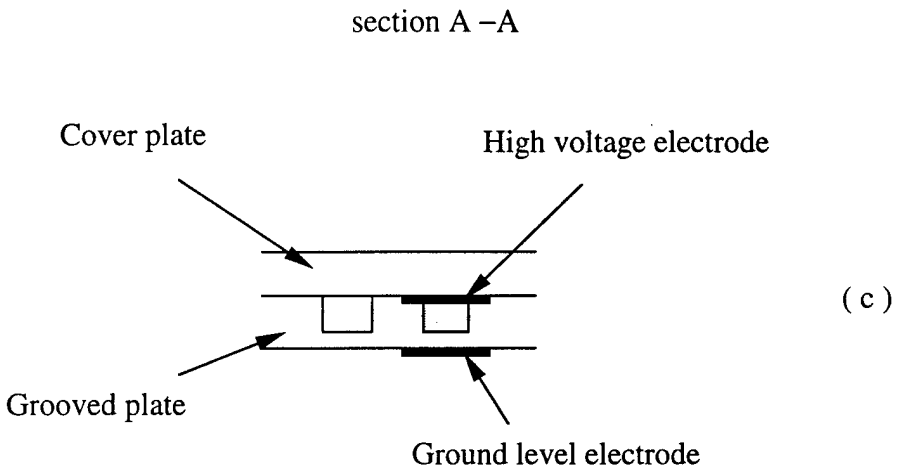

Figure 1. The schematic configuration of the EHD micro-heat pipes
(a) The configuration without application of electric field
(b) The configuration with application of electric field
(c) Schematic of the sandwich electrode structure at A-A section

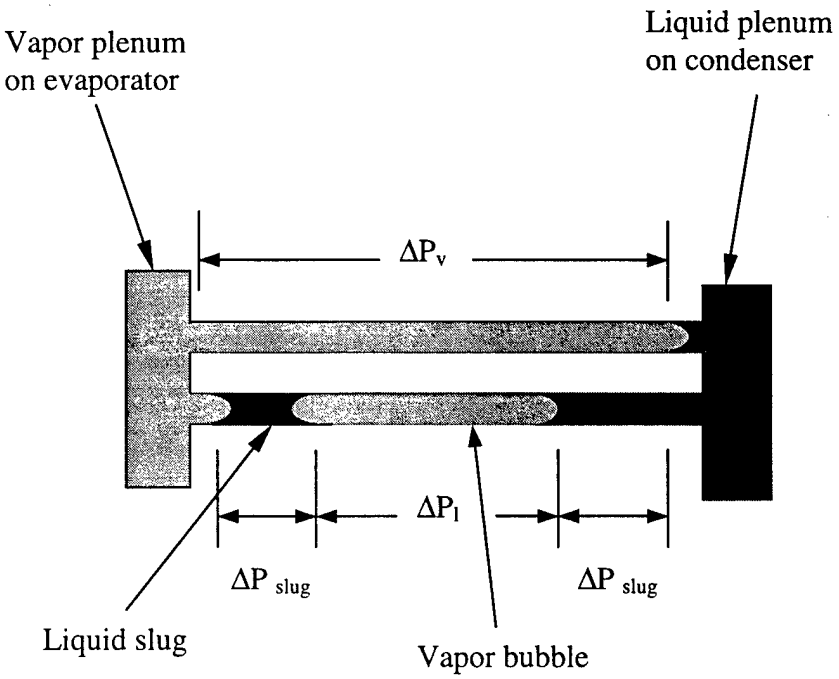

Figure 2. Illustration of the pressure drops distribution

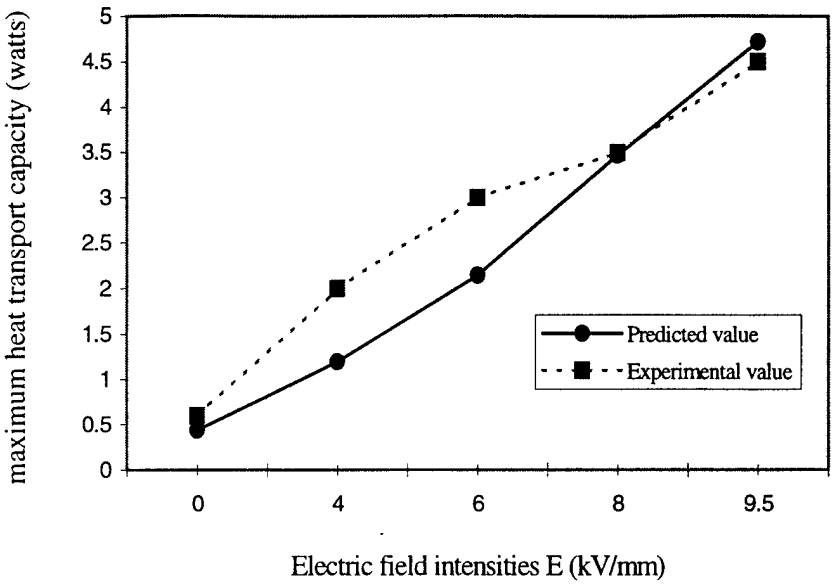

Figure 3 The predicted and the experimental maximum heat transport capacity versus electric field intensity

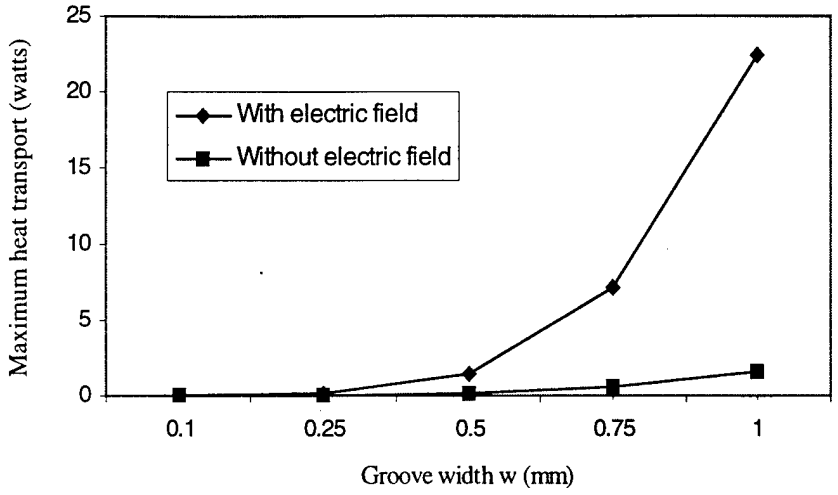

Figure 4 Theoretical maximum heat transport capacity for a single channel versus groove width with and without an applied electric field of 8 kV/mm

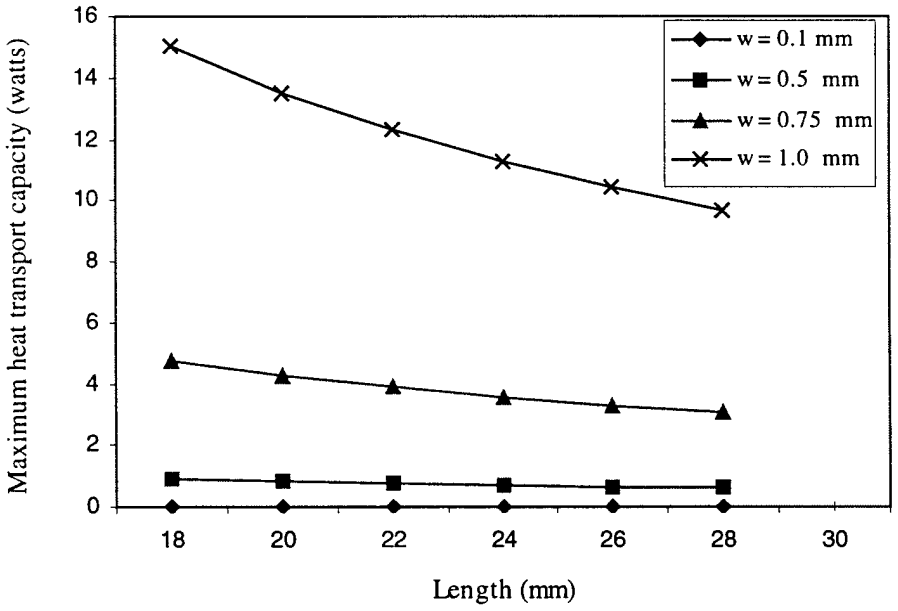

Figure 5 Theoretical maximum heat transport capacity versus length of the pipe with various groove widths at 8 kV/mm

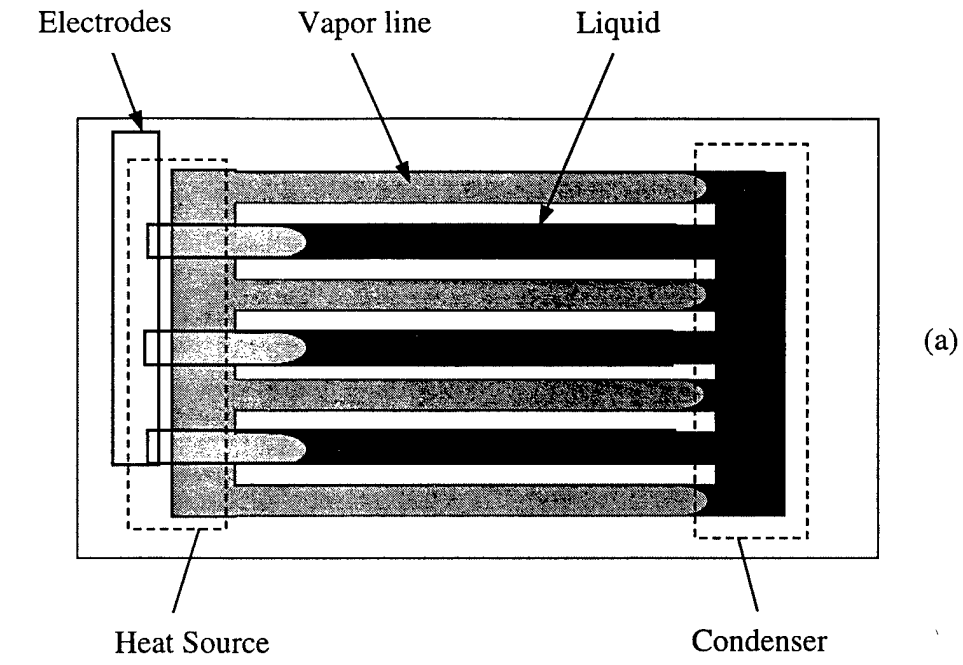

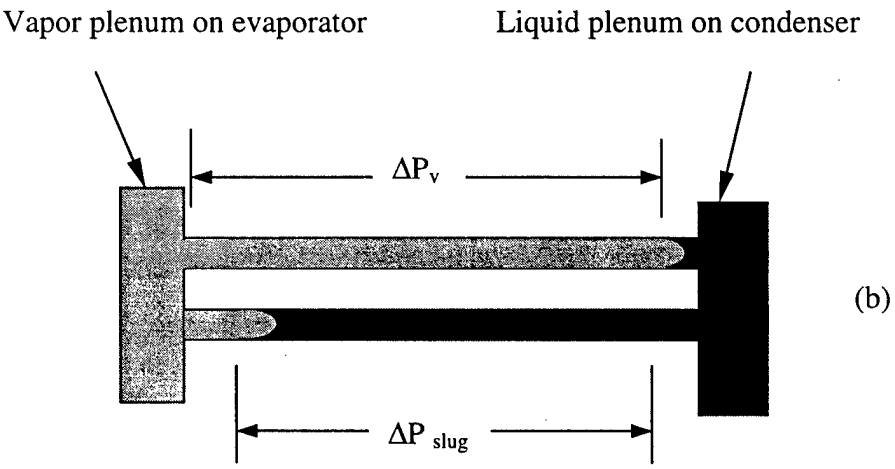

Figure 6 (a) Liquid fully filled schematic (the ideal model)
(b) Pressure drops in liquid fully filled case

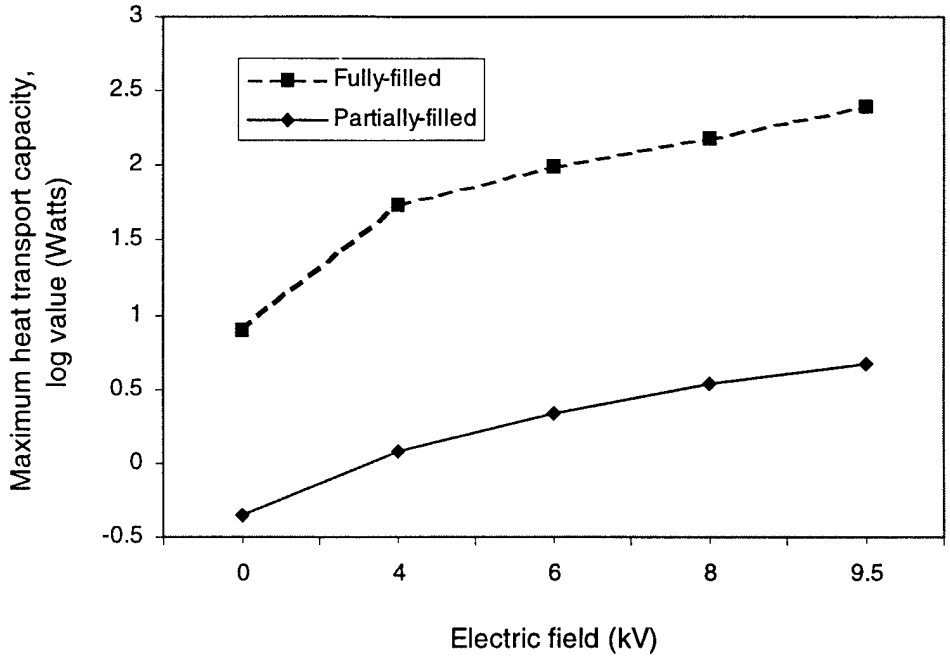

Figure 7 Predictions of maximum heat transfer capacity (log value) versus electric field for a fully-liquid filled and partially liquid filled evaporator

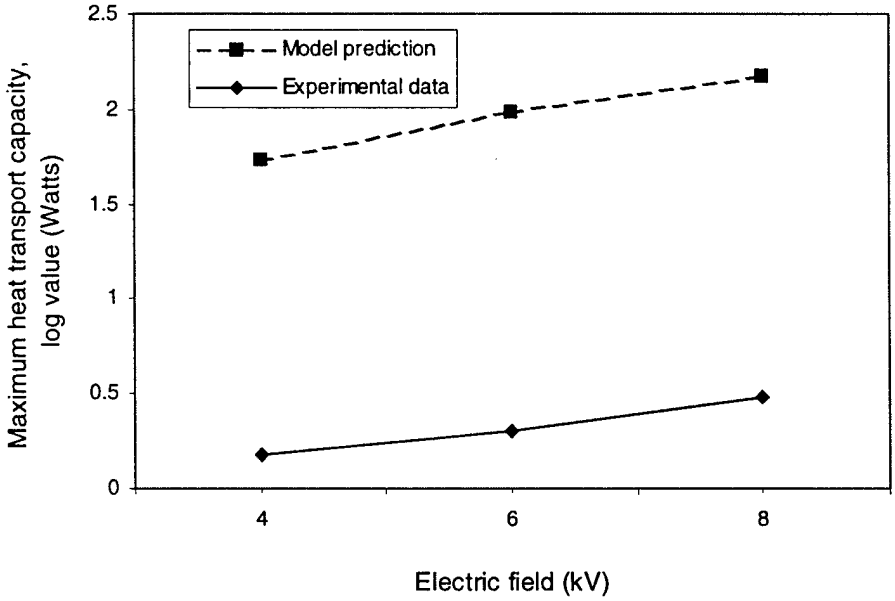

Figure 8 The maximum heat transport capacity (log value) for fully-liquid filled evaporator channel, prediction and the experiment data

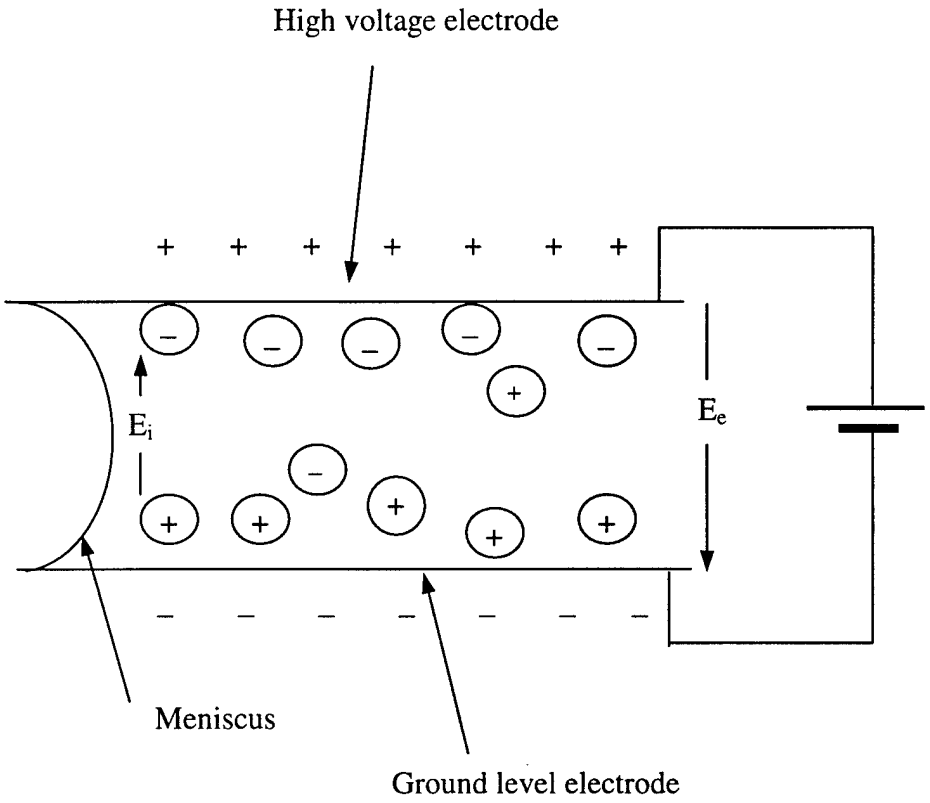

Figure 9 Schematic of the electric double layer

Table 1. The ratio of EHD driving potential and capillary pressure potential to the total driving potential

Electric field intensity (kV/mm)	$\Delta P_{electr} / \Delta P_{total}$	$\Delta P_{cap} / \Delta P_{total}$
0	0	100 %
4	63.3 %	36.7 %
6	79.5 %	20.5 %
8	87.3 %	12.7 %
9.5	90.7 %	9.3 %

Active Thermal Control of An Ion-drag Pump Assisted Micro Heat Pipe

Abstract

An ion-drag pump is utilized to enhance the heat transport capacity of micro heat pipes. An analytical model is developed to estimate the maximum heat transport capacity as a function of the applied electric field. The model demonstrates that four times increase in heat transport capacity is made possible through application of an electric field. The model predictions are shown to match experimental data well. Given the potential for augmentation of heat transport capability, a transient analytical model was developed to permit variation of the electric field with applied thermal load. A proportional-integral-derivative controller was used to simulate active temperature control. The feasibility of achieving the active temperature control was demonstrated experimentally.

Introduction

Effective thermal management for high temperature electronics are becoming more concerned. High temperature can cause electronics performance to degrade or cause it to fail prematurely. Faster speeds generate more heat, while smaller packages increase the difficulty of removing it from the devices that are adversely affected by increase temperature. The surface heat flux at the chip level for a 5 mm by 5 mm chip dissipating 10 W is 4×10^5 W/m^2 (McCluskey et al. 1997). Developing a high intensity heat dissipating system in micro scale is of significance for meeting not only the performance requirements, but reliability requirements as well. Micro heat pipe has shown its distinct feature in the passive management of the heat dissipation. However, the requirement of extremely high power dissipating of the high speed running electronics and the requirement of dynamic control of the temperature make the conventional micro heat pipe incompetent. Electrohydrodynamically assisted micro heat pipe becomes noticeable due to its high capability of intensity heat dissipation and active controllable nature. Among electrohydrodynamic pumps, ion-drag pump shows increasing potential. The configuration of ion drag pump is illustrated in Fig. 1 and the operation of the pump is as following. As Fig. 1 shown, an electric field is established between the negatively energized emitter and the grounded collector. Free charges are generated within the dielectric fluid by emission of the emitter as a corona source and then are dragged towards the collector. The friction between the moving charges and the working fluid creates a driving potential thus setting the fluid in motion.

Most of theoretical studies of the ion drag pump are based on the analyses provided by Stuetzer (1959). Stuetzer established a theoretical model based on Gauss' Law and derived the relation between pressure and electric field intensity

$$P\text{-}P_0 = (\varepsilon/2)\cdot(E^2 - E_0^2) \qquad (1)$$

where P is the pressure within fluid, ε the permittivity and E the electric field intensity. Based upon this relation he also developed the relations between operating voltage and pressure for cylindrical and spherical coordinate systems. Experiments were conducted to measure the pressure differences using corona point emitter as an ion source. It was found that for a corona point ion emitter the largest pressure buildup takes place in the immediate environment of the point. This model approximately matched the results of the experiments for static conditions. Stuetzer (1960) later discussed the dynamic situation. He used a loop system to measure the pressure drops within the moving fluid and derived an approximate expression relating dynamic pressure to the constant operating voltage involving pressure drop. The power efficiency of the pump system was also discussed.

Later, Pickard (1963a) provided more insight on the efficiency of pressure generation of ion drag pump and proposed the concept of "cut-in" voltage. He considered hydrodynamic instabilities as well. He concluded that below the "cut-in" voltage the pump is inoperative and above it the pump generated a pressure of the form $P \sim (V-V_0)^2$. He demonstrated that pressure instabilities occurred for constant voltage due to random fluctuations in emission.

Pickard (1963b) performed experiments to investigate the factors influencing ion pumping. It was found that suitable electrode-liquid combinations could produce better results. Acetone turned to be suitable liquid because it possesses a relatively high permittivity ($\varepsilon \approx 20$) and it can be readily purified. Molybdenum was found to be a suitable electrode material. The pressure instability occurring in his experiments was found to lead to undesirable short-term oscillations. He suggested three causes for the instability: the formation of a vapor pocket, hydrodynamic effects of the fluid velocity-generated pressure interrelationship and variations in pumping efficiency. A damping plug was inserted to the pump channel to damp-out the instability. Ac pumping was also tested, and he concluded that pumping was normally a multiionic process and that to obtain a maximum pressure head it was necessary to insure one electrode generates more charges than the other. The pitted anode surface in his experiments indicated a strong localized emission of ions in the experiments. Therefore, he discussed the electrode aging effects. In addition, the results of his experiments demonstrated that the measured current and the magnitude of the observed pumping bore no necessary connection. This is different from the Stuetzer's conclusion.

The basic assumption in the derivation of Stuetzer's and Pickard's model is using two plane-parallel electrodes to approximate the wire grid electrodes in practice. This means the variation of charge density around point-shaped emitter was neglected. Finally, they derived the maximum pressure as

$$P_{\max} = \frac{9}{8}\varepsilon \cdot \left(\frac{V}{d}\right)^2 \qquad (2)$$

where d is the spacing of the electrodes.

Based on Gauss's Law, Woodson and Melcher (1968) derived an expression describing charge density variation with the distance of emitter and electric Reynolds number. Using the Maxwell stress tensor, the pressure difference between the electrodes was given by $P(d) - P(0) = 1/2\varepsilon_0 [E^2(d) - E^2(0)]$, and finally yielded

$$P(d) - P(0) = \frac{\varepsilon_0}{2}\left(\frac{v_0}{b}\right)^2\left[-1+\left(1+\frac{2}{\mathrm{Re}}\right)^{1/2}\right]^2 \qquad (3)$$

Here $\mathrm{Re} = \varepsilon_0 v_0/(\rho_0 bd)$ is the electric Reynolds number, where v_0 is the velocity of charges at the emitter and ρ_0 is the initial charge density at the emitter. They demonstrated that the electric pressure was limited by the breakdown strength of the dielectric medium. Hence they suggested that magnetic field was able to provide higher pressure than electric field.

Crowley (1986) introduced a basic understanding of ion-drag force from an electrostatics point of view. In light of the Coulomb's force present, he developed a force density inside ion-drag pump:

$$F = \frac{\rho_0 V_0}{d} + \frac{\rho_0^2}{\varepsilon}\left(x - \frac{d}{2}\right) \qquad (4)$$

and the net force developed

$$f = \rho_0 A V_0$$

Then he derived the maximum pressure as

$$P_{\max} = \frac{2\varepsilon V_0^{\,2}}{d^{\,2}} \quad (\mathrm{N/m^2}) \qquad (5)$$

It is noted that the maximum pressure given by Eq.(5) is much larger than that of Stuetzer and Packard given by Eq.(2). Eq. (5) is also an approximation since many assumptions were made. And the primary assumption is that the electric field is uniform. In practice, the electric field is distorted, which makes problems more complicated. Eq. (4) indicates that a nonuniform pressure exists within fluid because of the variation of force density F with the distance x from the emitter. Therefore, an internal stirring of the fluid exists, forming electroconvection, which can reduce the output pressure.

Babin, Peterson and Seyed-Yagoobi (1993) developed an analytical model by simply applying Crowley's formula $\Delta P_{EHD} = \rho_0 V$ to the expression $\Delta P_c + \Delta P_{EHD} \geq \Delta P_v + \Delta P_l + \Delta P_g$ to evaluate the heat transport capacity of an ion drag assisted micro heat pipe. Here ΔP_c is the capillary pumping pressure, ΔP_{EHD} is the pumping pressure provided by the ion-drag pump, ΔP_v is the pressure required to transport the vapor from the evaporator to the condenser, ΔP_l is the pressure required to transport the liquid from the condenser to evaporator and ΔP_g is the hydrostatic pressure due to the local gravitational acceleration. Charge density ρ_0 is determined by $\rho_0 \leq (2\varepsilon V/d^2)$, which is Crowley's formula described in Eq. (5). Only the maximum pumping pressure can approximately be estimated through this relation. They constructed a two-stage ion-pump and conducted an experimental investigation to verify their analytical model. Both the results predicted by the model and obtained from experiments showed that the pressure generated by the ion-drag pump increased linearly with increasing voltage. Their results also showed that the slope of the predicted curve is approximately 10% less than that of the experimental curve. However, they did not establish the relation between heat transport capacity and operating voltage.

More recently, Bryan and Seyed-Yagoobi (1994) built an ion-drag pump with screen type electrodes occupying entire pipe cross section. Although they use Maxwell shear stress to derive two-dimensional electrical force, the final developed model is one dimensional. Combining the derived electric force with the momentum equation and

Gauss's law, after non-dimensionalizing, they solved the equations using a semi-implicit method. The profile of bulk liquid velocity via applied voltage was obtained. Three nondimensional electrical parameters were used in their analyses. They are electric Reynolds number $Re_E = \varepsilon U/(\sigma_e L)$, electric source number $E_{sl} = bV_0/(LU)$ and $E_s = \rho_0 L^2/\varepsilon V_0$. Here L is the spacing of electrodes. The electric field distribution along the pump axis was determined. It was found that electric source, Es, considerably influences the electric field distribution since it represents the magnitude of the charge injection at the emitter. As Es increases the gradient of the electric field increases, resulting in an increased flow rate.

Later, Seyed-Yagoobi, el al. (1995) further refined their analytical model. Their results were presented in terms of three nondimensional electric parameters, Re_E, Esl and Es. The results demonstrated that higher electric Reynolds number, Re_E, made a more uniform charge density distribution due to the longer charge relaxation time $\tau_e = \varepsilon/\sigma_e$ (recall $Re_E = \varepsilon U/(\sigma_e L)$). However, the data showed that electric slip number Esl played the most critical role in the distribution of charge density. Higher Re_E also resulted in larger gradient of nondimensional electric field. All the results showed low electric slip number made efficient operation of an
ion-drag pump. Further insight indicated that low conductivity and mobility and high permittivity resulted in high efficiency.

The present research applies the results of previous researcher to the development of a theoretical model capable of predicting the performance and the operational characteristics of an ion drag pump enhanced micro heat pipe device. An active feedback control model is also developed to simulate the use of the ion drag pump as a vehicle for achieving active thermal control of heated surfaces subject to transient thermal loads.

Theoretical Prediction of Maximum Heat Transport

The assumptions employed in the model development are: steady-state flow, one – dimensional electric field distribution, only one kind of ion (positive), constant fluid properties, constant surface tension and perfectly wetting liquid. Turbulence in the fluid is neglected.

The geometry of the ion-drag pump assisted micro heat pipes is shown in Fig. 1. In Fig. 1 (a), the collector is connected to ground level and the emitter to the negative high voltage level. When the electric field is applied, ions are generated in the neighborhood of the emitter within the dielectric liquid by emission of a discharge corona. The collector drags the ions and induces the motion of the liquid through the friction between moving ions and liquid forming the ion-drag pump. As shown in Fig.1 (b), the micro heat pipes are grooved in radial direction on the top surface and covered by a circular heated disc. The channels have a square cross section. The vertical supply channel in which the ion-drag pump is located possesses circular cross section. The ion-drag pump pushes the working liquid through the central hole into the micro heat pipes, as shown in Fig. 1 (c). Heat is added on the top of the device evaporating the working fluid. Condensation takes place in the surrounding annular region.

For the horizontal section of the device, i.e. micro heat pipe, the liquid control volume is selected as shown in Fig. 2. Here, $\dot{m}$ is the mass flow rate and

$$P_{l,x+dx} = P_{l,x} + \frac{dP_{l,x}}{dx}dx$$

$$\dot{m}_{l,x+dx} = \dot{m}_{l,x} + \frac{d\dot{m}_{l,x}}{dx}dx \tag{6}$$

The conservation of momentum in x direction for the liquid control volume requires

$$\left[\left(P_{l,x} + \frac{dP_{l,x}}{dx}dx\right)\left(A_{l,x} + \frac{dA_{l,x}}{dx}dx\right) - P_{l,x}A_{l,x}\right]$$

$$+\left[\left(\dot{m}_{l,x} + \frac{d\dot{m}_{l,x}}{dx}dx\right)\left(U_{l,x} + \frac{dU_{l,x}}{dx}dx\right) - \dot{m}_{l,x}U_{l,x}\right] + \tau_w 8r \cdot dx + \dot{m}'' \cdot 2\pi r \cdot dx = 0 \tag{7}$$

where $\dot{m}''$ is the momentum flux due to phase change at the interface. The frictional force in the horizontal channels is determined using the geometry in Fig. 3. The perimeter of the liquid phase is 8r, noting that r is the function of x. Here x = 0 is at the central point of the top evaporator region and x = L_h is at the condenser end of micro heat pipe. After some manipulation and neglecting higher order differential, Eq. (7) becomes

$$\frac{d}{dx}(P_{l,x}A_{l,x}) + \frac{d}{dx}(\dot{m}U_{l,x}) + \tau_w 8r + \dot{m}'' 2\pi r = 0 \tag{8}$$

Note that the first term includes the capillary pressure, expressed as

$$P_{l,c} = P_v - \frac{\sigma}{r} \tag{9}$$

In the present model, the primary portion of the pressure P results from the electrohydrodynamic pumping force. Therefore, the derivation of the relation between liquid driving pressure and EHD pumping force is of primary significance. The configuration of control volume in vertical section of the pump is illustrated in Fig. 4a. Here F_e is the electrohydrodynamic pumping force, F_w is the gravitative force and F_f is the frictional force. Assuming that there are N micro grooves and considering the vertical section and horizontal section as an whole control volume, a force balance is established on the control volume. The pumping pressure within the liquid flow is thus expressed as

$$P_l = \frac{1}{NA_p}(F_e - F_f - F_w) + \left(P_v - \frac{\sigma}{r}\right) \tag{10}$$

Here A_p is the vertical channel cross-section area, $\pi D_p{}^2/4$. The gravitative and frictional force are respectively defined as

$$F_w = \frac{\pi D_p^2}{4} \cdot L_p \cdot \rho_l g \tag{11}$$

$$F_f = \tau_w \cdot \pi D_p L_p \tag{12}$$

The electrohydrodynamic pumping force, F_e, is derived from the Maxwell stress tensor. It should be noted that the force acting on the charges is not just the form as might be expected from the basic form of electrostatic force equation: $F_e = \rho E$. This equation is

valid only for a vanishingly small volume of charges in an externally generated field. In present model, the charge distribution is not clear. Therefore, Maxwell stress tensor is used, which is valid for any charge distribution.

$$T_{ij} = \varepsilon E_i E_j - \frac{\varepsilon}{2}(E_k E_k)\delta_{ij} \tag{13}$$

where δ_{ij} is the Kronecker delta. The main electric field direction is in the vertical(y) direction, so the magnitude of E_x and E_z are much less than that of E_y. Thus the stress tensor is given as $T_{yy} = 1/2\ \varepsilon_l E^2 = P$. Therefore, F_e is defined as

$$F_e = \frac{1}{2}\varepsilon E^2 \cdot \frac{\pi D_p^{\ 2}}{4} \tag{14}$$

Substituting Eq. (11), (12) and (14) into Eq. (10) and rearranging yields

$$P_l = \frac{1}{N}\left(\frac{1}{2}\varepsilon_l E^2 - \tau_w \frac{4L_p}{D_p} - L_p \cdot \rho_l g\right) + \left(P_v - \frac{\sigma}{r}\right) \tag{15}$$

To compute the friction shear stress τ_w, the liquid flows in both the vertical section and horizontal section are assumed to be similar to fully developed duct flow. Thus the shear stress is expressed as (Bejan, 1995)

$$\tau_w = \frac{1}{2}\rho_l U_l^2 f \tag{16}$$

where f = k/Re. Here k is the parameter depending on the geometry of the channel (see Bejan, 1995). Reynolds number $Re = \rho_l U_{l,p} D_p / \mu_l$. Using the relation of the mass flow rate in the vertical channel $\dot{m}_p = \rho_l U_{l,p} A_p$, Eq. (16) becomes

$$\tau_{w,p} = \frac{2k_p \dot{m}_p \mu_l}{\pi \rho_l D_p^3} \tag{17}$$

For the horizontal section of the pump, the cross-sectional area of liquid flow can be determined in the light of Fig. 3

$$A_h = (4-\pi)\cdot r^2 \tag{18}$$

The hydraulic radius $r_{h,h}$ is defined as

$$r_{h,h} = \frac{2A_h}{p_h} = \frac{(4-\pi)\cdot r}{4} \tag{19}$$

where p_h is the wetted perimeter of the liquid flow.

Analogous to the derivation of Eq. (17) and using Eq. (19), noting that $Re = \rho_l U_{l,p} D_{h,h} / \mu_l$, where $D_{h,h}$ is the hydraulic diameter of the liquid flow and $r_{h,h} = D_{h,h}/2$, the frictional shear stress, τ_w, for the horizontal section is expressed as

$$\tau_{w,h} = \frac{k_h \dot{m}_h \mu_l}{\rho_l (4-\pi)^2 r^3} \tag{20}$$

Substituting Eq. (15), (17), (18) and (20) into (8) and using the relation of the mass flow rate in horizontal channel $\dot{m}_h = \rho_l U_h A_h$ and $\dot{m}'' = q''/h_{fg}$, where q'' is the heat flux,

yields the following equation

$$\left[\frac{2r}{N}\left(\frac{1}{2}\varepsilon_l E^2 - \frac{8k_p \dot{m}_p \mu_l L_p}{\pi\rho_l D_p^4} - \rho_l g L_p\right) + 2P_v r - \sigma\right](4-\pi)\frac{dr}{dx} + \frac{2\dot{m}_h}{\rho_l(4-\pi)\cdot r^2}\cdot\frac{d\dot{m}_h}{dx}$$

$$-\frac{2\dot{m}_h^2}{\rho_l(4-\pi)\cdot r^3}\cdot\frac{dr}{dx} + \frac{8k_h \dot{m}_h \mu_l}{\rho_l(4-\pi)^2\cdot r^2} + \frac{q''}{h_{fg}}\cdot 2\pi r = 0 \qquad (21).$$

In order to obtain nondimensional form, following nondimensionalizations are employed:

$$x^* = \frac{x}{L_h}; \qquad r^* = \frac{r}{w/2}; \qquad \dot{m}^* = \frac{\dot{m}_h}{\dot{m}_p/N}; \qquad (22)$$

Substituting Eq. (22) into (21) yields

$$\left[\frac{w}{N}\left(\frac{1}{2}\varepsilon_l E^2 - \frac{8k_p \dot{m}_p \mu_l L_p}{\pi\rho_l D_p^4} - \rho_l g L_p\right)\cdot r^* + P_v w\cdot r^* - \sigma\right](4-\pi)\frac{w}{2L_h}\cdot\frac{dr^*}{dx^*}$$

$$-\frac{8\dot{m}_p^2}{\rho_l(4-\pi)w^2N^2L_h\cdot r^{*3}}\cdot\dot{m}^{*2}\cdot\frac{dr^*}{dx^*} - \frac{8\dot{m}_p^2}{\rho_l(4-\pi)w^2N^2L_h\cdot r^{*2}}\cdot\dot{m}^*\cdot\frac{d\dot{m}^*}{dx^*}$$

$$+\frac{32k_h \dot{m}_p \mu_l}{\rho_l(4-\pi)^2 w^2 N\cdot r^{*2}}\cdot\dot{m}^* - \pi w\frac{q''}{h_{fg}}\cdot r^* = 0 \qquad (23)$$

In order to solve Eq. (23) numerically, the following assumptions and boundary conditions are employed: (1) $\dot{m}_h = \dot{m}_p/N$ at x = 0; (2) $\dot{m}_p$ is initially estimated by considering a force balance on the vertical channel.

$$\dot{m}_p = \frac{\rho_l \pi D_p^4}{8k_p L_p \mu_l}\cdot\left(\frac{1}{2}\varepsilon_l E^2 - \rho_l g L_p\right) \qquad (24)$$

(3) At the maximum heat transport condition dry-out occurs at x = L, and thus $r^* = w/2$ at $x^* = 0$ and $r^* = 0$ at $x^* = 1$; (4) P_v is determined as the saturate pressure associated with the local temperature. Finally Eq. (23) is solved subject to a conservation of mass constraint, requiring

$$\frac{d\dot{m}}{dx} = -\frac{q''}{h_{fg}} \qquad (25)$$

A solution to this system of Equations is obtained using fourth order Runge-Kutta method. Newtons' method is employed to iterate on $\dot{m}_p$ convergence is achieved.

Experiment

The schematic experimental apparatus is shown in Fig. 1. The diameter of the vertical is 0.003175 m. the spacing of the electrodes is 0.01 m. The width of the micro heat pipe is 0.001 m and the length is 0.005 m. There were eight such channels. The working fluid used is n-Pentane. The amount of the working liquid is large enough to maintain its temperature constant in the experimental process, that is, room temperature. The temperature of the heat source was measured using thermistor. Heat was input via an electric resistance heater element located on the top of the system. The applied electric field was fixed at 15 kV/mm level.

Results and Discussion

The maximum heat flux of the experiment at 15 kV/mm is 40 W/cm^2 at steady state, which is obtained for the maximum electric field achievable before electric breakdown is shown.

Sample model calculations are presented in Figs. 5 and 6. It should be recognized that for a given electric field E, the maximum heat input flux q'' is achieved when both r^* and $\dot{m}^*$ reach zero at $x^* = 1$, since under these conditions all working liquid within the micro heat pipes is evaporated into vapor without dryout occurring. The predicted maximum q'' is presented as a function of electric field, as shown in Fig. 7. This figure clearly indicates that the applied electric field plays a significant role in the performance of ion-drag assisted micro heat pipe. Increasing electric field intensity can increase the maximum heat transport capability noticeably. A similar trend was observed by Bryan and Yagoobi (1994). Experimental results is also depicted in Fig. 7. Good correspondence prediction and experiment is obtained

The geometry of a micro heat pipe generally has significant influence on its heat transport capability. Therefore, predictions are made to demonstrate the influence of geometry variations of the heat transport capacity. These results are presented in Figs. 8 and 9. Fig. 8 shows that the width of micro heat pipe channels has a large influence on the maximum heat transfer capability. It is suggested that roughly $q''_{max} \propto w^3$, which agrees with the results from other studies conducted by Longtin et al. (1994) and Yu et al. (2000). Fig. 9 illustrates the effect of the length of micro heat pipe. It is seen that the maximum heat transfer capacity decreases linearly with an increased micro heat pipe length. These results further confirm the recommendations of Longtin et al that short and wide channel produces optimum heat transfer.

The effect of the spacing of the electrodes and the diameter of the vertical channels on the liquid driving pressure of the micro heat pipe are evaluated. The results do not show noticeable influences from them. Therefore, these effects are negligible.

Controlling of the EHD Pump

The most promising feature of the EHD pump to the micro heat pipe is the application of active temperature control. The feasibility of heat transport capability augmentation demonstrated by previous results leads the possibility of achieving thermal control for transient heat-loadings. The control is implemented through the control of electric field intensity and thereby controlling the mass flow rate of the working liquid. The governing equation is

$$q(t)_{input} - q(t)_{evap} = C_p \frac{d}{dt}(m_b T) \tag{26}$$

where q_{input} is the heat input, q_{evap} is the heat to be evaporated, and m_b and C_p are respectively the mass and specific heat of the heated substrate. For evaporation, q_{evap} can be expressed as

$$q_{evap} = \dot{m} h_{fg} \tag{27}$$

In the EHD micro heat pipe, the mass flow rate $\dot{m}$ is determined by the applied electric field E, namely, $\dot{m} = m$ (E). Thus Eq. (26) can be

$$q(t)_{input} - \dot{m}(E) h_{fg} = C_p \frac{d}{dt}(m_b T) \tag{28}$$

Applying the Laplace transformation on Eq. (28) yields

$$T(s) = \frac{q(s) - \dot{m}(E) \cdot h_{fg}}{C_p m_b s} \tag{29}$$

where s is the Laplace variable. This latter relationship presumes that the flow field responds much more quickly than the temperature filed since it uses $\dot{m}(E)$ as calculated using Eq. (23). Eq. (29) is solved using the Matlab simulink environment and the control block diagram is presented in Fig. 12. The control operation procedure is as following. The temperature of the heat source is measured and compared with the reference temperature. If the temperature of the heat source is higher than the reference one, the micro-controller will turn on the EHD pump at certain electric field level. Certain amount of working fluid will be provided into the evaporator region to cool down the region and obtain the desired temperature in the region. Once the heat source temperature is lower than the reference one, the micro-controller will turn off the EHD pump.

Simulation and Experimental Results with Active Thermal Control

The corresponding transient response is presented in Fig. 13. It is seen that after several oscillations (120 seconds), the temperature reached steady state at required temperature. The heat input was chosen as a pulse pattern in order to simulate the actual situation in electronic components. The duty cycle was selected from 70% to 100%. The heat input control was simulated using Pspice software, and the diagram of the schematics was shown in Fig. 14. After all the control models were verified by computer simulation, the physical facility was built up and the experiment was implemented.

Experiments were performed on the controlled ion-drag pump. The electric field was generated by a high voltage power supply (Model: PS/LG-10 P 15). The heat was generated by a resistance heater and controlled through the control circuit. The reference temperatures were set to be 63 ^{0}C, 68 ^{0}C, 87 ^{0}C and 89 ^{0}C respectively. The P. I. D. controller controls the on-off duty cycle. When the temperature reached above the reference temperature, the micro controller would turn on the electric field, and ion drag pump was started to cool down the heat source.

Two of typical plots that recorded the variations of temperature versus time under control condition are presented in Figs. 13 and 14. It can be seen that the heat control system effectively controlled the temperature of the system according to the reference temperature. Fig. 14 shows that if no electric field, the temperature will go up fast and reaches very high level. While the applied electric field makes the temperature go down quickly and keep it at lower level. It is also noted that although the heat input (26 W/cm^2) in Fig. 13 is higher than that in Fig. 14 (17 W/cm^2), the control system can control the temperature depending on the requirement. The control of the magnitude of the temperature oscillation can be achieved by adjusting the duty cycles of the electric field pulse, that is, the ratio of on time to off time. It can be seen from Fig. 14 that through enlarging the duty cycle or increasing the frequency of the duty cycle, the electric field is applied intensively. The temperature is thereby almost kept as constant, $90.5 \pm 0.5\ ^0C$. Therefore, the control of the temperature can be carried out more precisely. In the comparison of Fig. 13 with Fig. 14, it is apparent that high frequency can make the control of temperature more precise than the effect of long duty cycle. Hence high frequency is demanded in precise case.

Conclusion

An analytical model is developed on the ion drag pump assisted micro heat pipe. The interfacial effects, the interfacial radius of curvature and the change of flow direction are taken into account in the model development. Nondimensionalization are employed. The resulting differential equation is solved numerically. The model predictions show that the heat transport capacity increases with the increase of the intensity of the electric field. This is due to the increase of both the amount of emitted free charges and the velocity of these charges. The evaluation of the ion drag pump geometry does not show significant influence on the performance. Some of the model predictions agree with the experimental results from other studies.

Temperature control is achieved by the control of electric field. This is the noticeable feature of this system that distinct from the other heat dissipating system. A desired temperature is maintained through controlling the electric field. High frequency can make a precise temperature control.

Nomenclature

A = cross-sectional area, (m^2)
b = the mobility of the ion
C_p = specific heat of the fluid, (J/kg·K)
D = diameter of the channel, m
d = the spacing of the electrodes, m
E = electric field intensity, (V/m)
f = friction factor
g = gravitational acceleration, (m/s^2)
h_{fg} = latent heat of vaporization, (kJ/kg)
L = length, m

m = mass of the working fluid, kg

$\dot{m}$ = mass flow rate, (kg/s)

P = pressure, (N/m^2)

q = heat transport, Watts

Re = Reynolds number

r = the curvature radius of liquid-vapor interface, m

T = temperature, K

w = channel width, m

U = the velocity of flow, m/s

V = the operating voltage, Volt

ε = permittivity

ρ = density, (kg/m^3)

σ = surface tension, N/m

σ_e = the conductivity

λ = latent heat of vaporization, (J/kg)

μ = viscosity, (Ns/m^2)

ψ = tilt angle

τ_w = shear stress

Subscripts

c = capillary

e = electric

h = horizontal section

h = hydraulic

l = liquid

max = maximum

p = vertical section

v = vapor

Reference

Babin, B. R., Peterson, G. P., and Seyed-Yagoobi, J., 1993, "Experimental Investigation of an Ion-Drag Pump-Assisted Capillary Loop", Journal of Thermophysics and Heat Transfer, Vol. 7, No. 2, pp. 340-345.

Bejan, A., 1995, *Convection Heat Transfer*, John Wiley & Sons, New York, pp. 100-105.

Bryan, J. E., and Seyed-Yagoobi, J., 1994, "Analysis of 2-dimensional Flow Field Generated by a 1-Elecrode-pair Ion-drag Pump", IEEE Transactions on Dielectrics and Electrical Insulation, Vol. 1, No. 3, pp. 459-467.

Crowley, J.M., 1986, *Fundamentals of Applied Electrostatics*, John Wiley & Sons, New York, pp.153-156.

Longtin, J. P., Badran, B., and Gerner, F. M., 1994, "A One-Dimensional Model of a Micro Heat Pipe During Steady-State Operation", Journal of Heat Transfer, Vol. 116, pp. 709-715.

McCluskey, F. P., Grzybowski, R., and Podlesak, T., 1997, *High Temperature Electronics*, CRC Press, New York, pp.Chapter 7.

Pickard, W. F., 1963a, "Ion Drag Pumping. I. Theory", Journal of Applied Physics, Vol. 34 No. 2, pp. 246-250.

Pickard, W. F., 1963b, "Ion Drag Pumping. II. Experiments", Journal of Applied Physics, Vol. 34 No. 2, pp. 251-258.

Seyed-Yagoobi, J., 1995, "Theoretical Analysis of Ion-Drag Pumping", IEEE Transactions on Industry Applications, Vol. 31, No. 3, pp. 469-476.

Stuetzer, O. M., 1959, "Ion Drag Pressure Generation", Journal of Applied Physics, Vol. 30, No. 7, pp. 984-994.

Stuetzer, O. M., 1960, "Ion Drag Pumps", Journal of Applied Physics, Vol. 31 No. 1, pp. 136-146.

Woodson, H. H., and Melcher, J. R., 1968, *Electromechanical Dynamics*, John Wiley & Sons, New York, pp. 776-783.

Yu, Z., Hallinan, K., Bhagat, W., and Kashani, R., 2000, "Experimental and Analytical Studies of the Maximum Heat Transport Capacity in Electrohydrodynamically Enhanced Micro Heat Pipes", 34th National Heat Transfer Conference in Pittsburgh, Aug. 2000.

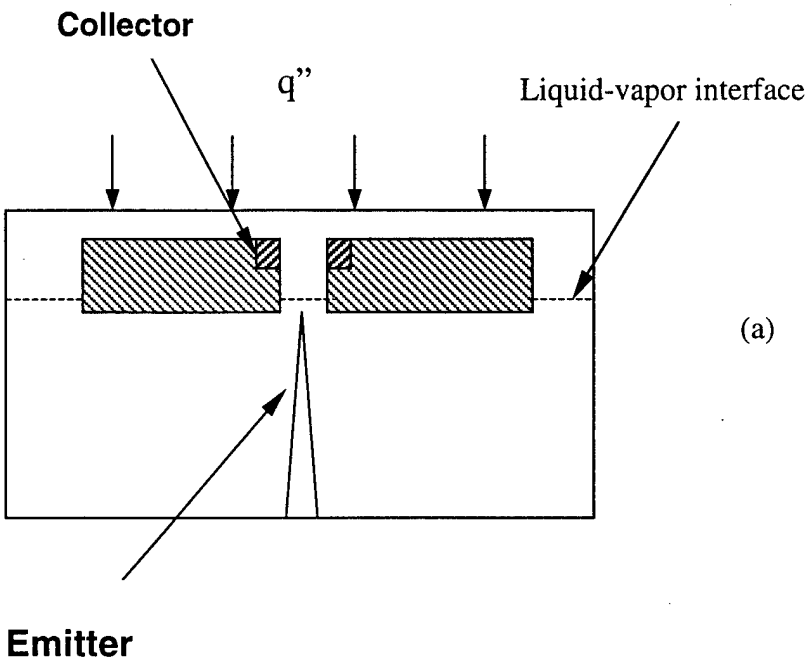
Collector
q"
Liquid-vapor interface
Emitter

(a)

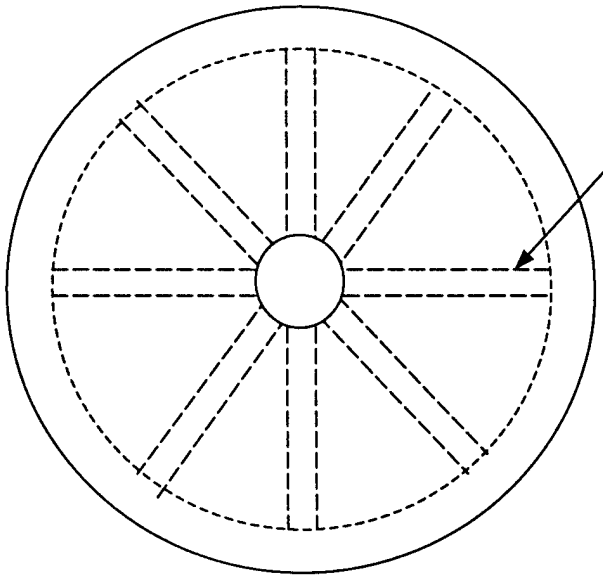
Micro heat pipe

(b)

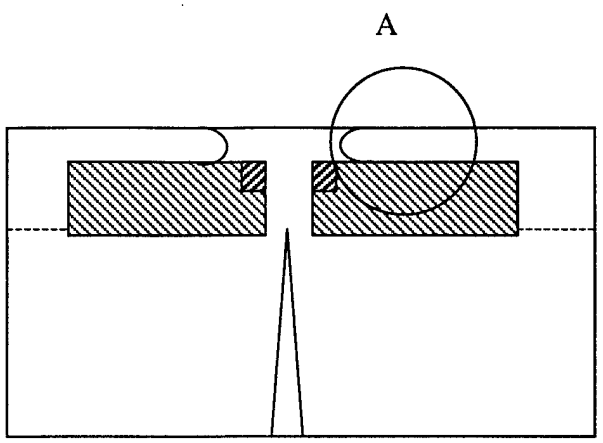

(c)

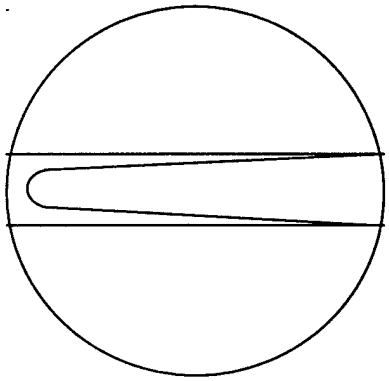

Detail of A

Figure 1 The geometry of the ion-drag pump assisted micro heat pipes
(a) The schematic of the system without electric field
(b) The look-down configuration of the system
(c) The configuration with electric field

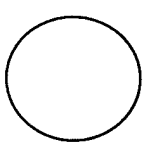

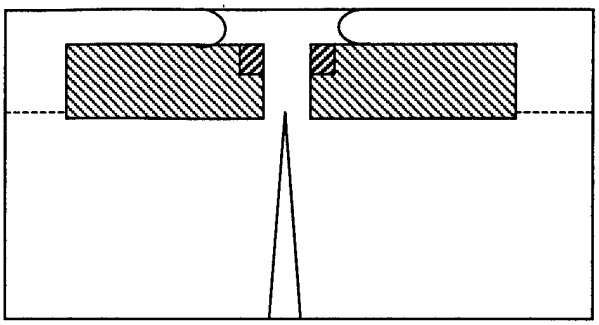

(a)

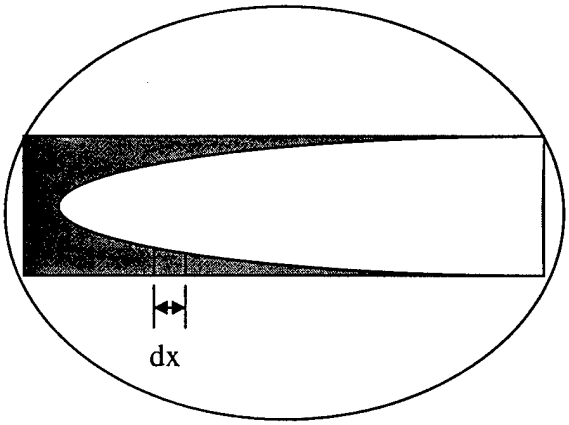

Detail of A

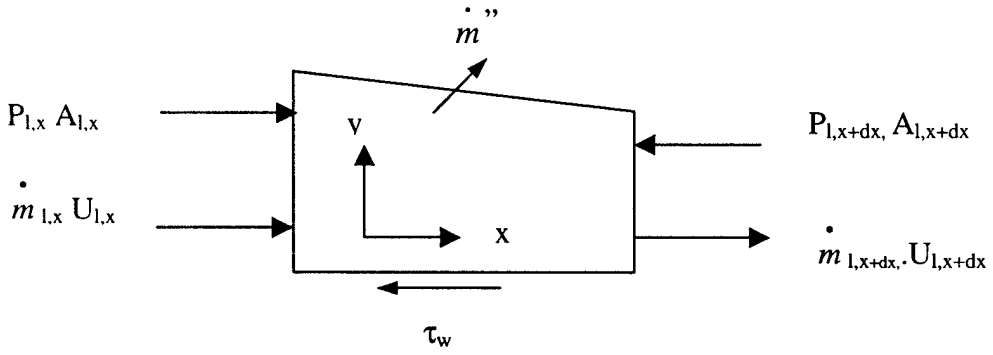

(b)

Figure 2 (a) Schematic of a micro heat pipe
(b) Control volume

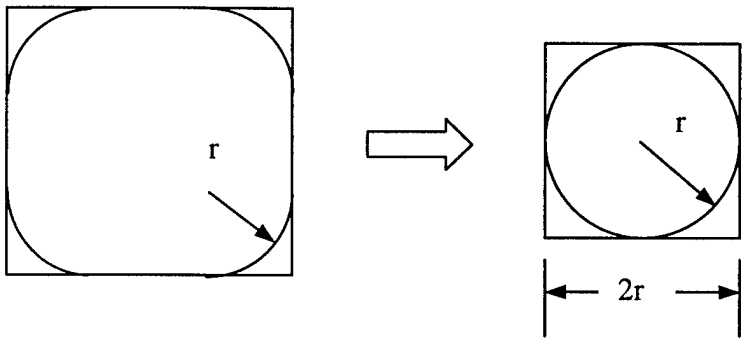

Figure 3 The geometry of the cross-section area of liquid flow within the micro heat pipe at x.

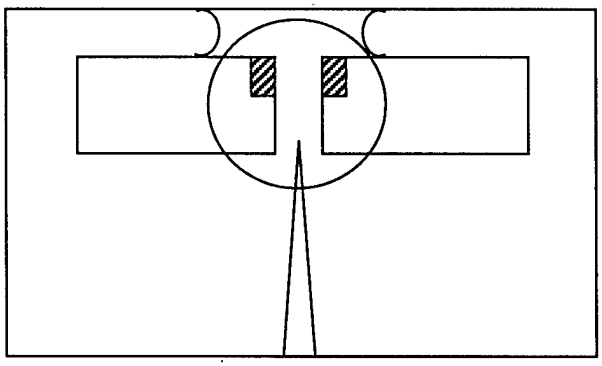

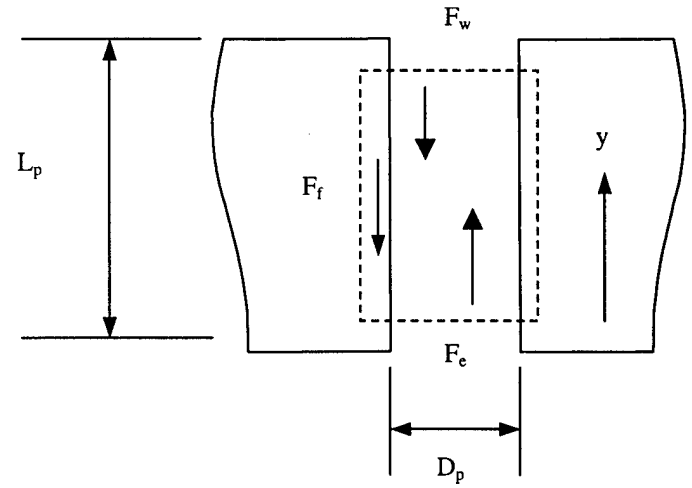

(a)

Control volume 1:

Vertical channel

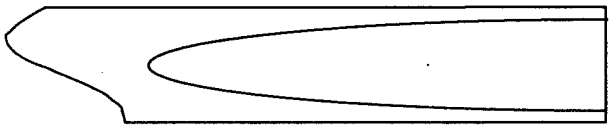

(b)

Control volume 2:

Horizontal channel

Figure 4 Configuration of the control volume

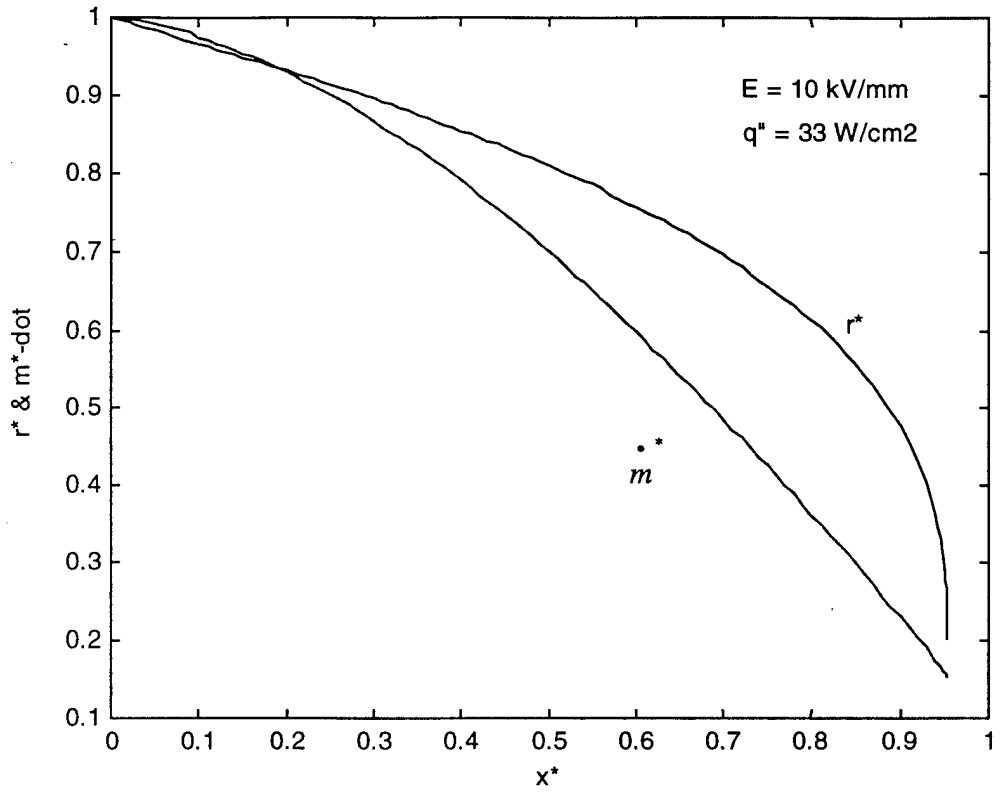

Figure 5 The profiles of the calculation results at 10 kV/mm, heat input: 33 W/cm^2

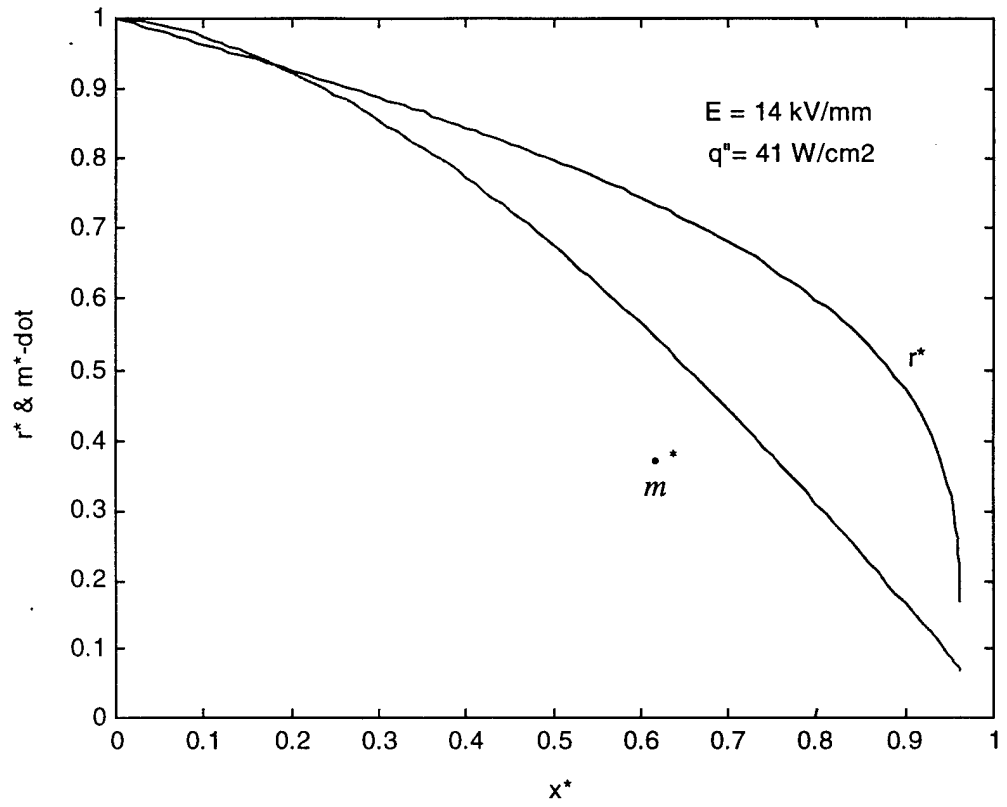

Figure 6 The profiles of the calculation results at 14 kV/mm, heat input: 41 W/cm^2

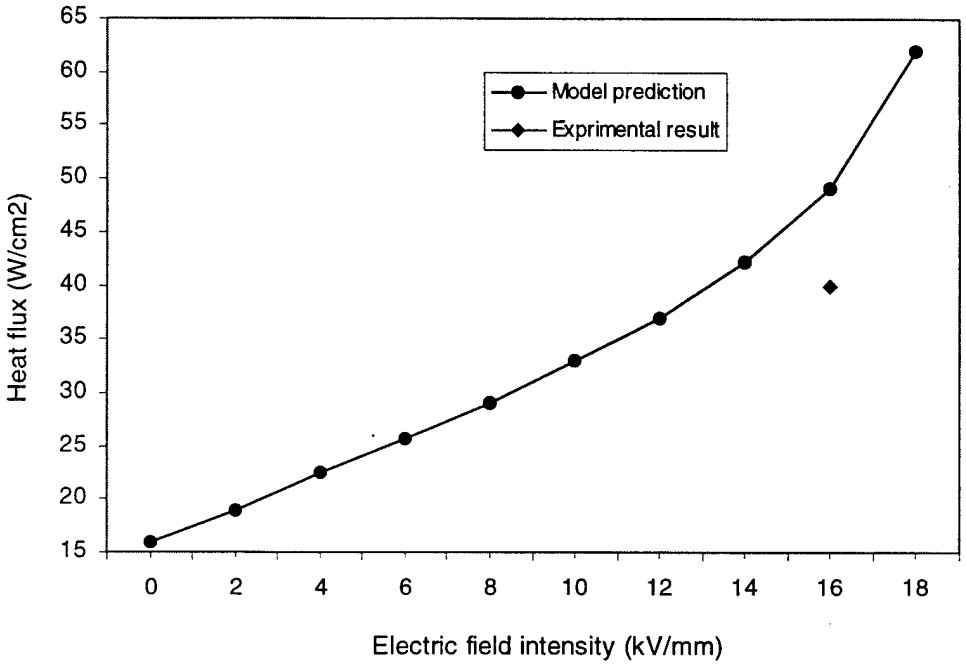

Figure 7 The maximum heat transport capacity versus the applied electric field

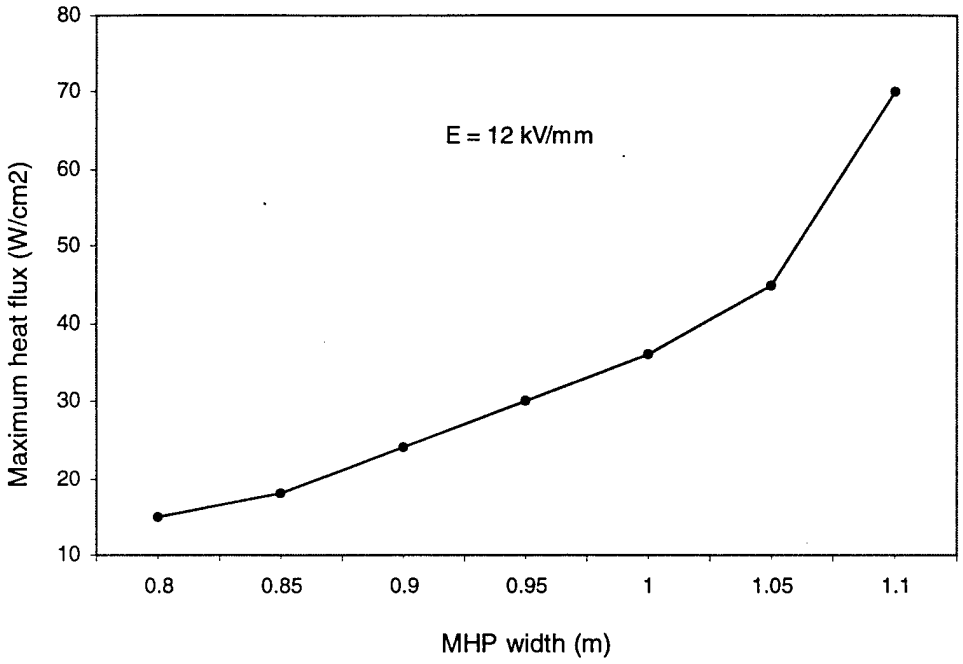

Figure 8 Heat flux capacity versus the width of micro heat pipe

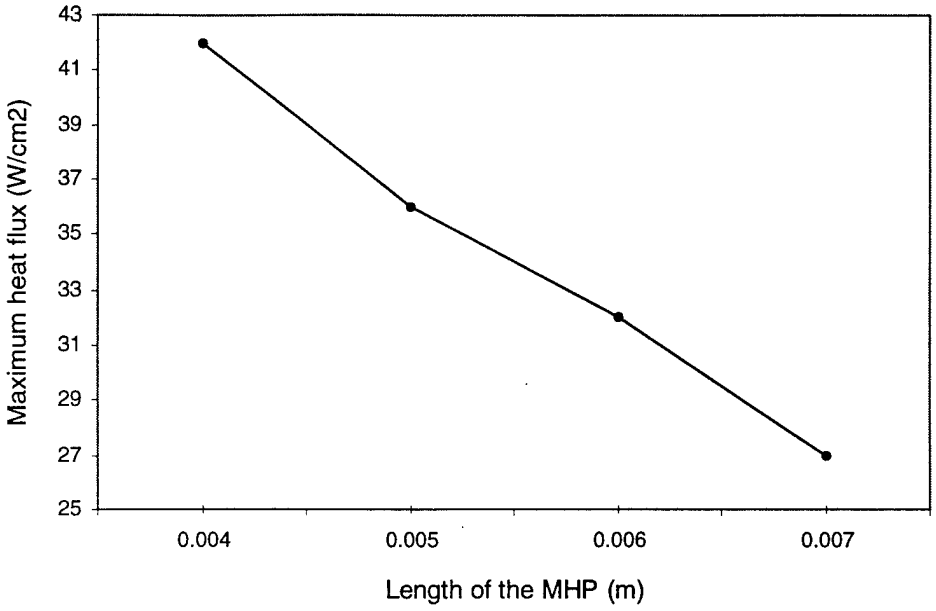

Figure 9 Heat flux capacity versus the length of micro heat pipe

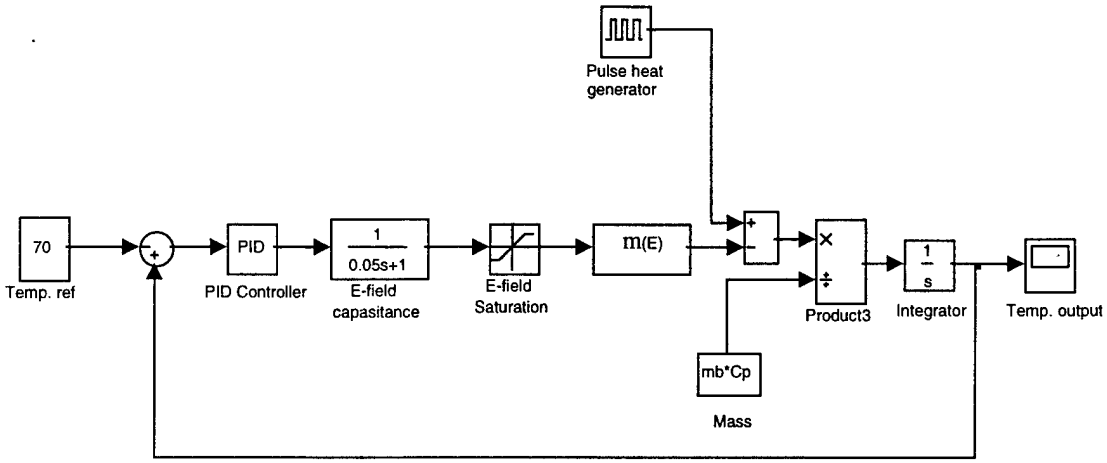

Figure 10 Diagram of control simulink blocks

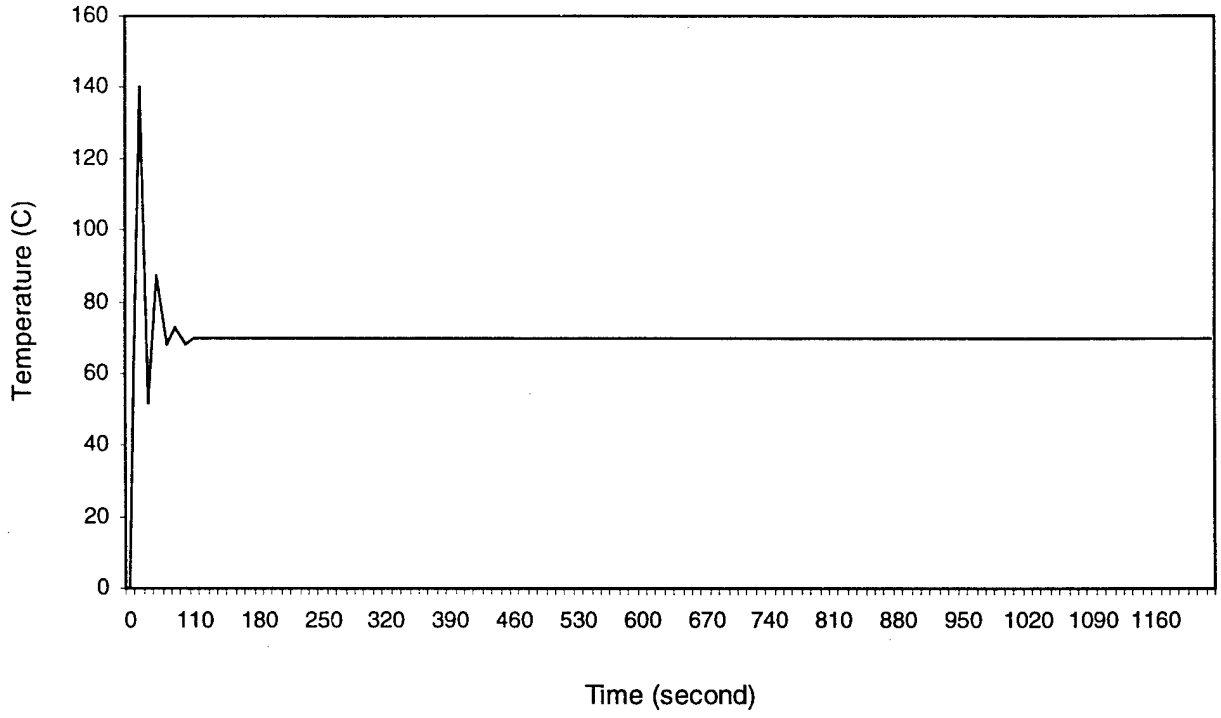

Figure 11 Temperature response of control simulink

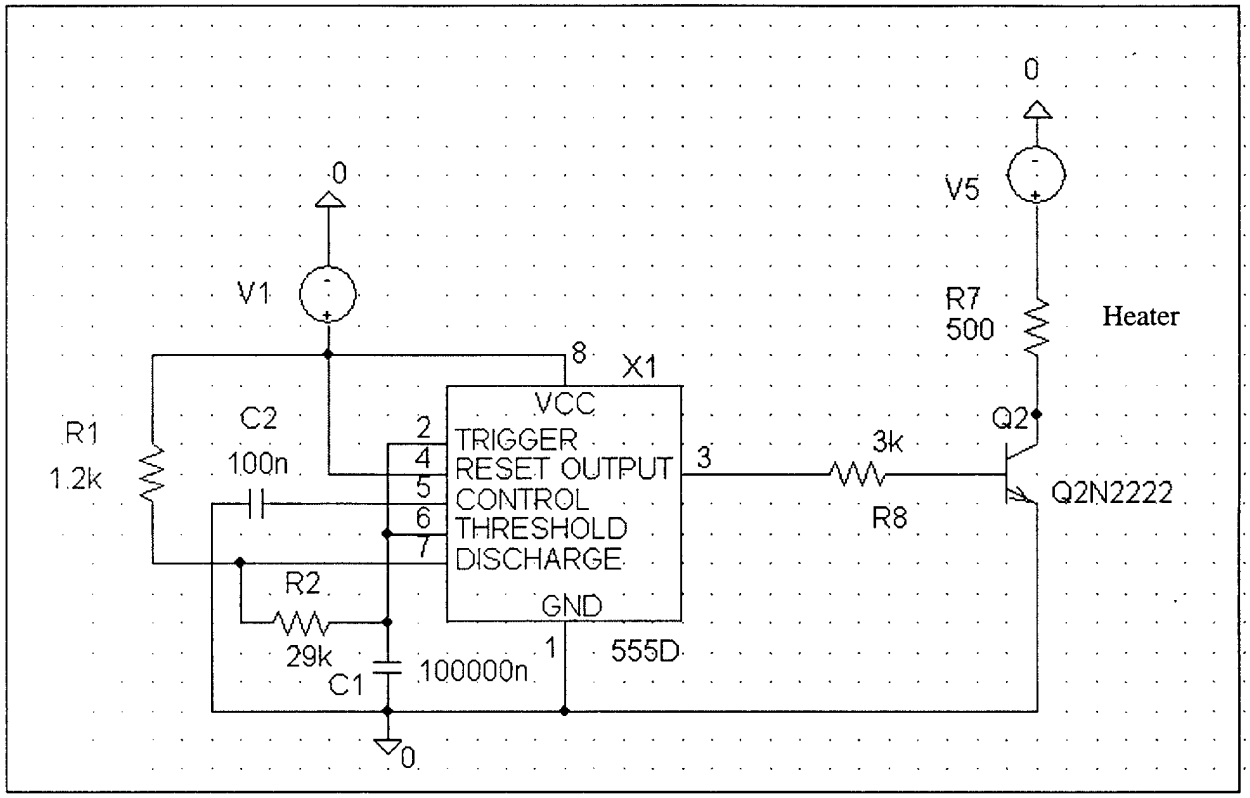

Figure 12 Schematics of pulse heat generating circuit

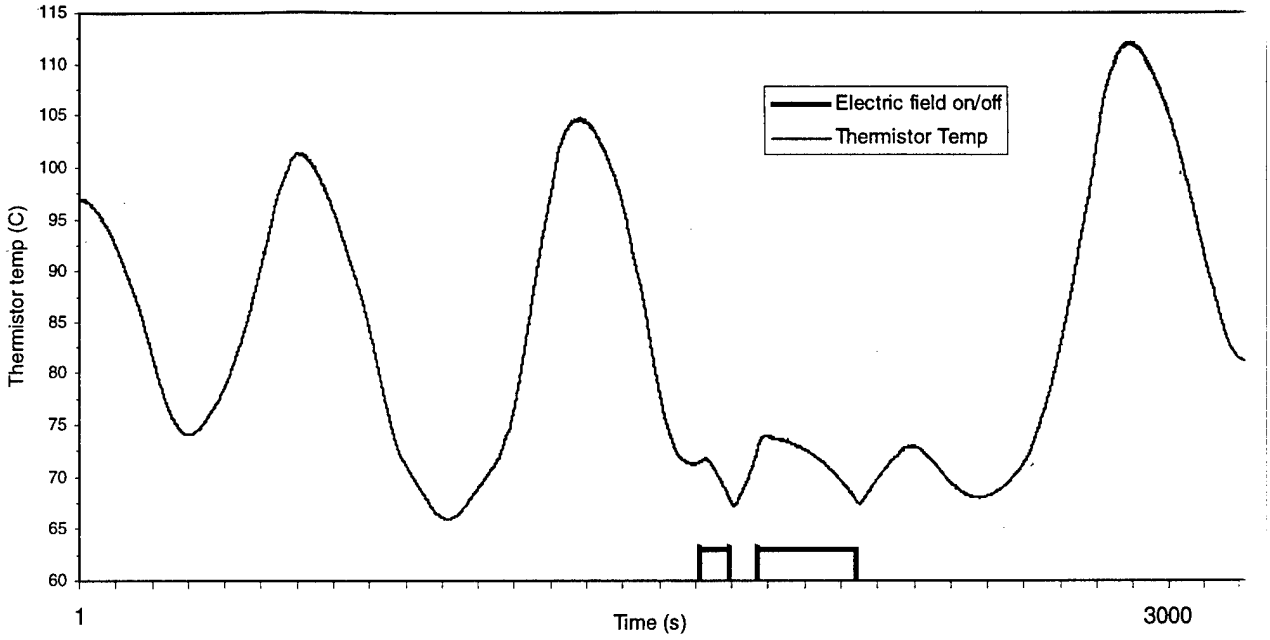

Figure 13 Temperature variation versus time at 15 kV/mm, heat flux: 40 W/cm^2 and reference temperature: 63 ^{0}C

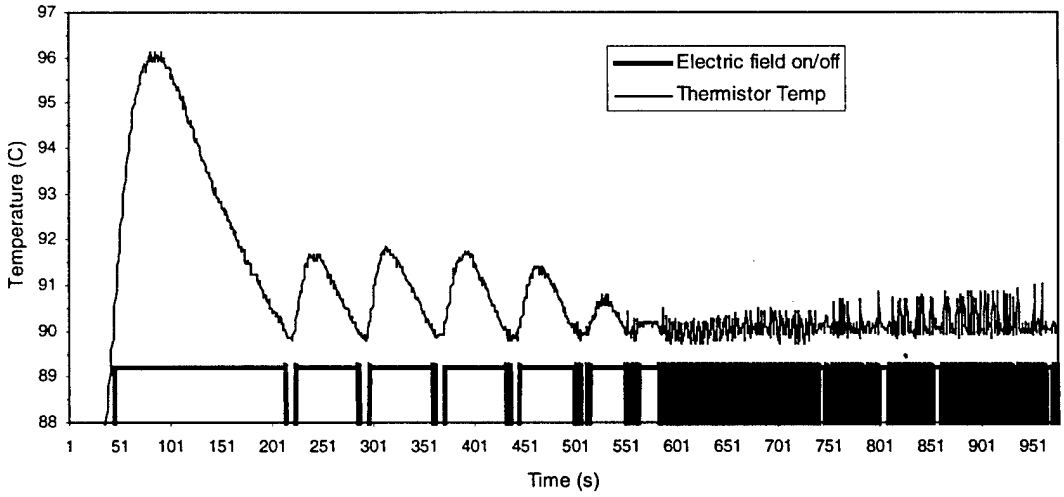

Figure 14 Temperature variation versus time at 15 kV/mm, heat flux: 40 W/cm^2 and reference temperature: 89.3 ^{0}C.